Basin Research

IAS EAGE

Basin Research (2018) **30**, 544–563, doi: 10.1111/bre.12264

Topographic growth of the Jishi Shan and its impact on basin and hydrology evolution, NE Tibetan Plateau

Joel E. Saylor,* Jessica C. Jordan,†,[1] Kurt E. Sundell,* Xiaoming Wang,‡ Shiqi Wang§,¶ and Tao Deng§

**Department of Earth and Atmospheric Sciences, University of Houston, Houston, TX, USA*
†School of Earth Sciences and Environmental Sustainability, Northern Arizona University, Flagstaff, AZ, USA
‡Department of Vertebrate Paleontology, Natural History Museum of Los Angeles County, Los Angeles, CA, USA
§Key Laboratory of Vertebrate Evolution and Human Origins, Institute of Vertebrate Paleontology and Paleoanthropology, Chinese Academy of Sciences, Beijing,China
¶Center for Excellence in Tibetan Plateau Earth Sciences, Chinese Academy of Sciences, Beijing, China

ABSTRACT

Previous research demonstrates that large basins on the periphery of the northern edge of the Tibetan Plateau were partitioned during development of intrabasin mountain ranges. These topographic barriers segregated basins with respect to surface flow and atmospheric circulation, ponded sediments, and formed rain shadows. However, complex mixing between airmasses and nonsystematic isotope-elevation lapse rates have hampered application of quantitative paleoaltimetry to determine the timing of development of critical topographic barriers. We address the timing and drivers for changes in surface connectivity and atmospheric circulation in the Linxia and Xunhua basins using a multidisciplinary approach incorporating detrital zircon geochronology, Monte Carlo inverse flexural modelling, and published stable isotope data. Disruption of surface flow between the two basins during exhumation of the Jishi Shan preceded development of topography sufficient to intercept moisture-bearing airmasses. Detrital zircon data point to disruption of an eastward-flowing axial fluvial network between 14.7 and 13.1 Ma, coincident with the onset of exhumation in the Jishi Shan. Flexural modelling suggests that by 13 Ma, the Jishi Shan had developed 0.3 ± 0.1 km of relief; sufficient to disrupt eastward-flowing drainage networks but insufficient to intercept moisture-bearing airmasses. Stable isotope data indicate that, although surface connections between the Xunhua and Linxia basins were broken, the two basins continued to be dominated by a common climate regime until 9.3 Ma. Subsequent reintegration of surface flow between the basins occurred between 9.3 and 7.6 Ma. Divergence in the stable isotope and depositional environment records between the two basins suggests that at 9.3 Ma the paleo-Yellow River breached the growing Jishi Shan dam, and may have reintegrated surface flow between the two basins via erosion of the modern Yellow River gorge, which transects the Jishi Shan. The reintegration of the Xunhua and Linxia basins' surface connection is confirmed by reintroduction of a Songpan-Ganzi flysch sediment source by 7.6 Ma. Continued exhumation and uplift of the Jishi Shan developed 0.8 ± 0.2 km of relief by *ca.* 8 Ma capable of intercepting moisture-bearing airmasses; isolating and increasing aridity in the Xunhua Basin while decreasing it in the Linxia Basin. Our findings point to protracted development of the modern *ca.* 1 km of relief in the Jishi Shan between 14 and *ca.* 4.5 Ma followed by attainment of a topographic equilibrium which persists into modern times.

Correspondence: Joel E. Saylor, Department of Earth and Atmospheric Sciences, University of Houston, Houston, TX 77204, USA. E-mail: jesaylor@uh.edu
[1]Present address: Pioneer Natural Resources, Irving, TX 75039, USA

INTRODUCTION

Regional surface uplift and growth of basin-bounding mountain ranges are inextricably linked to regional and local paleoenvironmental change in the northern Tibetan Plateau (Dettman *et al.*, 2003; Kent-Corson *et al.*, 2009; Hough *et al.*, 2014; Zhuang *et al.*, 2014; Li *et al.*, 2016). Upward and outward growth of the Tibetan Plateau has been linked to simultaneous weakening of Indian Summer Monsoon circulation and strengthening of East Asian Monsoon circulation (An *et al.*, 2001; Tang *et al.*, 2013). The northeastern Tibetan Plateau is characterized by formation and subsequent partitioning of large peripheral basins (Metivier *et al.*, 1998; Meyer *et al.*, 1998; Tapponnier *et al.*, 2001; Horton *et al.*, 2004; Carroll *et al.*, 2010; Craddock *et al.*, 2011; Horton, 2012; Bush *et al.*, 2016). Exhumation and uplift of new basin-bounding ranges formed topographic barriers to surface flow and atmospheric circulation, promoting arid rainshadow conditions within the new sub-basins (Sobel *et al.*, 2003; Strecker *et al.*, 2007; Hough *et al.*, 2014; Pingel *et al.*, 2014). Following surface uplift, formation of basin-margin topographic barriers and associated arid conditions inhibited erosional evacuation and resulted in sediment ponding. However, the current exposure of basin fill in many northeastern Tibetan Plateau basins points to a subsequent period of drainage integration and sediment evacuation (Fang *et al.*, 2003; Garzione *et al.*, 2005; Lease *et al.*, 2007, 2012a; Craddock *et al.*, 2011; Liu *et al.*, 2013; Hough *et al.*, 2014).

Despite the importance of understanding the elevation history of the northeastern Tibetan Plateau on monsoon strength and aridity trends in central Asia, reconstructing the paleoelevation of basin-bounding mountain ranges remains difficult for several reasons. First, the *in situ* geochemical proxies that might be used to reconstruct paleoelevation are often not preserved at high elevations due to erosion, and it is the mountain ranges that block moisture-bearing air masses and whose paleoelevation must be determined. Second, application of stable isotopic lapse rates to quantitatively reconstruct paleoelevation is subject to multiple complicating factors (e.g. Quade *et al.*, 2007, 2011; Leier *et al.*, 2009; Botsyun *et al.*, 2016). Complicating factors most relevant to the northeast Tibetan Plateau include extensive recycling of southern-derived moisture during advection over the mass of the Tibetan Plateau, subcloud evaporation in arid settings, mixing of multiple moisture sources including the East Asian Monsoon and central Asian airmasses (Araguas-Araguas *et al.*, 1998; Tian *et al.*, 2001; Hren *et al.*, 2009; Bershaw *et al.*, 2012), and potentially the impact of climate change on stable isotopic lapse rates (Poulsen & Jeffery, 2011; Botsyun *et al.*, 2016). North of the Tibetan Plateau where moisture is dominantly sourced from the Atlantic Ocean precipitation $\delta^{18}O$ values are controlled primarily by seasonal temperature changes resulting in nonsystematic relationships between elevation and stable isotopic compositions (Tian *et al.*, 2007). Due to these complexities, the magnitude of surface uplift needed to drive regional or local changes in atmospheric circulation remains unconstrained.

Here, we determine the middle Miocene–Pliocene paleoelevation evolution of the basin-bounding Jishi Shan using a Monte Carlo approach to flexural modelling by evaluating the response of the Linxia Basin to random topographic loads (Fig. 1). Because flexural modelling yields nonunique solutions, the growth of topography, and surface and atmospheric connectivity is interpreted by comparison to new and published detrital zircon geochronology, thermochronology, and stable isotopic compositions of paleosol and lacustrine carbonates on both sides of the Jishi Shan. Flexural modelling indicates that the Jishi Shan developed *ca.* 75% of its modern relief between 13 and 7.6 Ma and resulted in disruption of atmospheric circulation patterns between the basins to the east and west of the range at *ca.* 8 Ma. Topographic growth was accompanied by cut-off of diagnostic southwest-derived detrital geochronology age modes at 13 Ma. Subsequent reintroduction of these characteristic source signatures by 7.6 Ma points to the establishment of the modern course of the Yellow River, which transects the Jishi Shan (Fig. 1).

GEOLOGICAL SETTING

Paleogene deformation and basin formation

Cenozoic deformation in the northeastern Tibetan Plateau occurs in an intraplate setting, more than 1,500 km from the nearest major plate boundary. Deformation in the region is dominated by two stages: 1) north-south–oriented contraction in the Paleogene–early Neogene and 2) east-west–oriented transpression in the middle Miocene–Pliocene. In the first stage, Paleogene formation of the regionally integrated Longzhong Basin in response to crustal loading by the West Qinling was followed by progressive dissection and isolation of subbasins in the Neogene (Craddock *et al.*, 2011; Lease *et al.*, 2011, 2012a; Yuan *et al.*, 2013; Lease, 2014). The West Qinling fault is a north-verging, west-northwest-trending, sinistral transpressional fault system on the southern edge of the Longzhong (now Linxia) Basin (Fig. 1b, GBGMR, 1989; QBGMR, 1991). Apatite (U-Th)/He data from the hanging wall of the West Qinling fault reveal rapid and major cooling at *ca.* 45–50 Ma followed by relatively minor cooling at 17–18 Ma, interpreted as two pulses of exhumation (Clark *et al.*, 2010). The West Qinling fault places

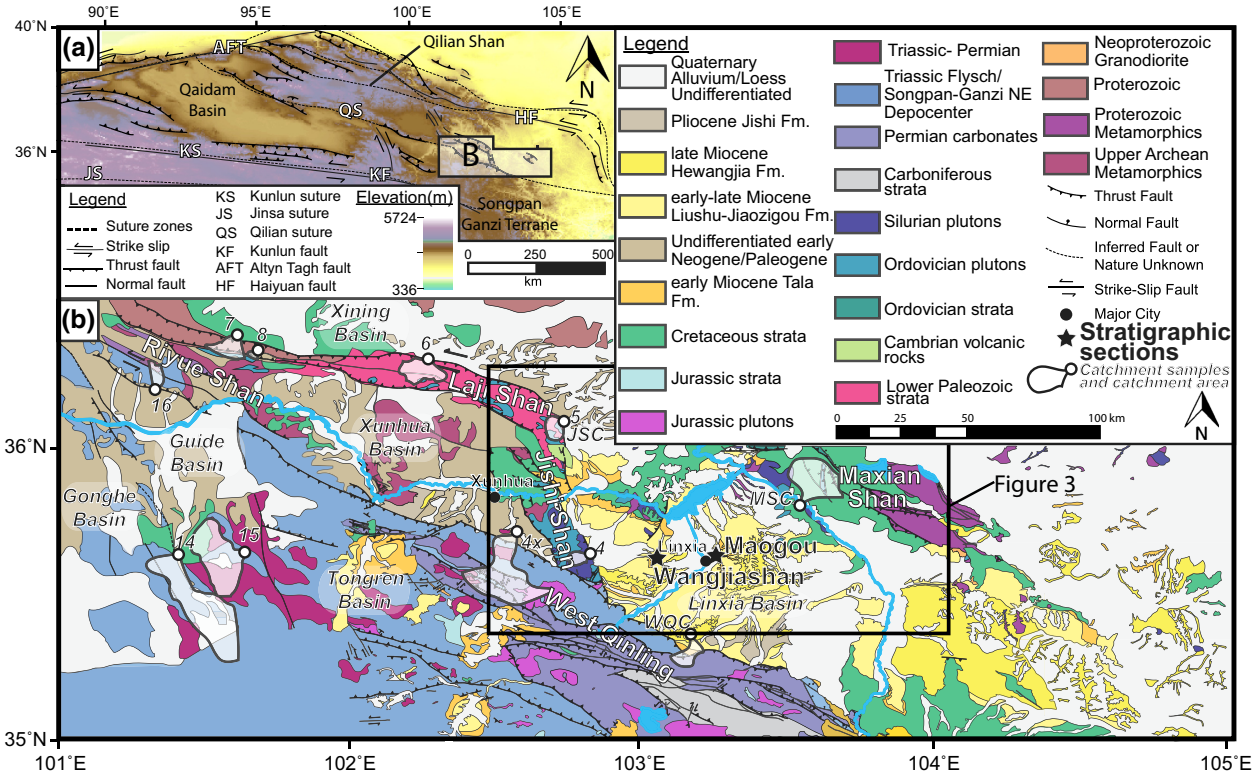

Fig. 1. (a) Digital elevation model of the northern Tibetan Plateau showing the location of the Linxia Basin relative to major tectonic elements of the northeastern Tibetan Plateau. Modified from DeCelles *et al.* (2007), Clark *et al.* (2010), Craddock *et al.* (2011) and Duvall *et al.* (2013). (b) Geologic map of the Linxia Basin region. Deposition of the Jishi through Tala formations is localized to Linxia basin, where present elsewhere indicates coeval deposition to the Linxia basin stratigraphy. Outlined numbered catchment samples are modified from Lease *et al.* (2007, 2012a), lettered samples are from this study. See Table S1 for details. Modified from Gansu Bureau of Geology and Mineral Resources (1989), Qinghai Bureau of Geology and Mineral Resources (1991), Weislogel *et al.* (2010), Hough *et al.*(2011), Lease *et al.* (2012a), and Liu *et al.*(2013).

Carboniferous–Permian carbonate rocks and banded siliceous limestone, Lower–Middle Triassic Songpan-Ganzi flysch, Lower Triassic volcanic rocks, Lower Triassic–Jurassic granite, and Cretaceous conglomerate in the hanging wall over Neogene strata of both the Linxia and Xunhua basins in the footwall to the north (Fig. 1b, QBGMR, 1991; Sun *et al.*, 1997). The West Qinling fault merges with faults bounding the Laji Shan in the Riyue Shan thrust belt west of the Xunhua Basin (QBGMR, 1991).

Neogene deformation and basin formation

Deformation migrated *ca.* 60 km northward at *ca.* 22 Ma with the exhumation of the east–west trending Laji Shan and Maxian Shan along a bivergent transpressional thrust system (Fig. 1b, Dayem *et al.*, 2009; Clark *et al.*, 2010; Duvall *et al.*, 2011; Lease *et al.*, 2011, 2012a). This exhumation and resultant rapid cooling persisted until *ca.* 15 Ma, after which it transitioned to a slower cooling rate, which is inferred to persist through modern times (Lease *et al.*, 2011). Exhumation of these mountain ranges disrupted the Longzhong Basin and isolated the Linxia/Xunhua basins to the south from the Xining Basin to the north (Lease *et al.*, 2011; Duvall *et al.*, 2013). The Laji Shan is composed of Proterozoic phyllite, schist and dolomite, Cambrian-Ordovician meta-andesite, Ordovician andesitic tuff and breccia interbedded with chert, slate and phyllite, Ordovician plutons, Cretaceous conglomerate, and Paleogene Xining Group conglomerate (QBGMR, 1991). The Maxian Shan is composed of Proterozoic metamorphic rocks, Neoproterozoic granodiorite, Paleozoic plutons, and Cretaceous and Jurassic strata (CGIRCUG, 2006a,b,b).

The second stage began in the middle Miocene when the Tibetan Plateau underwent an orogen-wide change in kinematics. On the northern margin of the plateau this change is marked by a transition from north-northeast–oriented contraction to east-east sinistral shear and transpressional faulting, while central Tibet accommodated both northward contraction and east-west extension along conjugate strike-slip faults (Taylor *et al.*, 2003; Lease *et al.*, 2011, 2012a; Duvall *et al.*, 2013; Yuan *et al.*, 2013). Separation of the previously contiguous Xunhua/Linxia

Basin into its two component basins during uplift of the Jishi Shan completed the partitioning of the single Longzhong Basin into multiple, isolated basins (Craddock *et al.*, 2011; Hough *et al.*, 2011).

The Linxia Basin is a flexural basin (Fang *et al.*, 2003) which formed initially in response to exhumation of the West Qinling (Clark *et al.*, 2010). However, Neogene subsidence in the Linxia Basin is driven primarily by loading by the north-trending Jishi Shan along range-bounding bivergent thrust systems (Fig. 1b, Fang *et al.*, 2003; Lease *et al.*, 2012b). Rapid exhumation in the Jishi Shan began at 13–14 Ma and has continued until the present (Lease *et al.*, 2011). Prior to 14 Ma the rocks in the hanging wall of the east-directed Jishi Shan thrust record slow cooling (Lease *et al.*, 2011). The west-directed thrust on the western flank of the range is known to have been active after 13 Ma based on deformed Xunhua Basin strata dated at 9.3 Ma and partially reset apatite (U-Th)/He ages as young as 8 Ma from a sample in the hanging wall (Lease *et al.*, 2012a). The northern third of the Jishi Shan is comprised primarily of Paleozoic metamorphic rocks locally intruded by Ordovician granite and overlain by Cretaceous conglomerate. A small swath of Cambrian volcanic rocks is present in the most northern portion of the Jishi Shan. Neoarchean–Paleoproterozoic schist and Cretaceous conglomerate dominate the central portion while lower Paleozoic plutons characterize the southern segment (Lease *et al.*, 2012a; Liu *et al.*, 2013).

METHODS

Measured stratigraphic sections

Linxia Basin-filling stratigraphy was measured at decimeter scale at two locations: Wangjiashan (35.628533° N, 103.058250° E) and Maogou (35.649383° N, 103.273317° E, Fig. 1b). We conduct subsidence analysis of the entire stratigraphic interval, but focus on the 14–2.6 Ma interval for flexural analysis. The stratigraphy was decompacted and backstripped using a MATLAB-based code developed by Nestor Cardozo (Cardozo, 2016) which implements standard decompaction and backstripping methods (Angevine *et al.*, 1990; Watts, 2001; Allen & Allen, 2005). Lakes in the Linxia Basin record are interpreted to be shallow and have minimal impact on subsidence analysis and therefore no water depth correction was applied. Decompaction accounts for sediment volume changes associated with mechanical decreases in porosity by calculating the exponential decrease in porosity with depth. Deposition of a veneer of Pleistocene loess of variable thickness would have minimal impact on sediment compaction and was not incorporated into the decompaction calculations. Clastic lithofacies are assigned a porosity coefficient (1/km in depth), surface porosity (%) and a grain density (kg/m^3) modified from Sclater & Christie (1980). Values for claystone are taken from those reported for shale by Sclater & Christie (1980) and values for siltstone are calculated assuming a linear mix of 75% sandstone and 25% shale from Sclater & Christie (1980). The surface porosity of siltstone is taken from Bond & Kominiz (1984) (Table S2).

Zircon U-Pb geochronology

Zircon U-Pb analyses were conducted primarily at the University of Houston. A subset of the samples was analysed at the LaserChron Center at the University of Arizona (see Data repository text for details of samples analysis and Table S1 for details of which samples were analysed at each location). Zircon grains were separated from fine- to coarse-grained sandstones following standard mineral separation procedures of crushing, disc milling, water tabling and heavy liquids and magnetic separation.

$^{207}Pb^*/^{206}Pb^*$ provides greatest precision for ages >1400 Ma, while $^{206}Pb^*/^{238}Pb$ is more precise for ages <1000 Ma. We place the cut-off between $^{207}Pb^*/^{206}Pb^*$ age and $^{206}Pb^*/^{238}Pb$ age between 900 and 1000 Ma to avoid bisecting grain populations (Gehrels *et al.*, 2008). Grains older than 600 Ma exhibiting greater than 20% discordance or less than −5% reverse discordance are discarded. A separate filter is applied to all grains younger than 600 Ma, such that grains whose 2σ uncertainty envelope does not overlap the 15% discord are removed from further consideration. Grains that pass these filters are plotted as probability density plots (PDPs) and histograms (Sircombe, 2004). Due to the possibility of Pb loss or core inheritance and the difficulty of interpreting (particularly young) slightly discordant ages when grains are not cogenetic, geologic interpretations are guided by age modes comprising at least three overlapping grain ages (Dickinson & Gehrels, 2008).

Comparison of detrital zircon age spectra is aided by multidimensional scaling (e.g. Vermeesch, 2013). Multidimensional scaling (MDS) of detrital zircon data attempts to transform the dissimilarity between samples to distance in N-dimensional space. Samples are represented as a point, typically in two-dimensional or three-dimensional Cartesian space, with greater distances between two points indicating greater dissimilarity between the two U-Pb age distributions. The transformation is accomplished by iterative rearrangement of the data in N-dimensional space to minimize the misfit ("stress") between the calculated distances and the disparities. Stress is calculated as $\left(\frac{\sum_{ij}\left(f\left(x_{ij}\right)-d_{ij}\right)^2}{\sum_{ij} d_{ij}^2}\right)^{0.5}$, where d_{ij} is the distance and $f(x_{ij})$

is the disparity between the ith and jth element. Disparity is calculated as a linear (1:1) transformation of the input dissimilarities. In a low-stress MDS plot, the distances between points linearly correlate with the dissimilarities between samples. Metric nonclassical MDS was implemented using an in-house MATLAB algorithm (Data S1 and S2). Dissimilarity was calculated as the Kuiper V value and the coefficient of nondetermination (calculated as the complement of the Cross-correlation coefficient: 1-R^2, Saylor *et al.*, 2012, 2013; Saylor & Sundell, 2016). Because the V value and coefficient of nondetermination are different and are calculated differently, the resulting MDS plots are not expected to be identical. Rather, the MDS plots are expected to yield consistent intersample distances, consistent up-section trends and complementary interpretations. Plots are interpreted in terms of relative up-section changes in similarity between samples and sources with greatest weight given to those trends seen in MDS plots derived from both metrics.

Flexural modelling

Flexural modelling was implemented using a MATLAB-based inverse Monte Carlo model to that calculates subsidence profiles from prescribed topographic loads of random sizes and densities (Data S3). The code incorporated two classes of models: lithosphere that is infinite in the x-direction and lithosphere that occupies a semi-infinite space in the x-direction (Fig. 2). In both cases the plate is assumed to extend infinitely in the z-direction (into the plane of the page), rendering the problem two-dimensional. The infinite lithosphere model incorporates equations modified from Wangen (2010) that calculates cumulative lithospheric flexure induced by multiple topographic loads. The deflection at each individual point is then the sum of the deflections due to N applied loads calculated as,

$$w(x) = \sum_{i=1}^{N} \frac{V_i}{2\,\Delta\rho\; g\; \alpha} f(u). \tag{1}$$

In Eqn. 1, $\Delta\rho$ is the difference in density between the displaced substrate (Fig. 2 ρ_s: mantle) and the material that fills the depression created by the applied load (Fig. 2 ρ_i: basin sediments). The variables g and α are the acceleration due to gravity and flexural parameter, respectively. The flexural parameter is calculated as

$$\alpha = \left[\frac{E\; T_e^{\,3}}{3\;\Delta\rho\; g\; (1-\nu^2)}\right]^{\frac{1}{4}}, \tag{2}$$

where E is Young's modulus, ν is Poisson's ratio and T_e is effective elastic thickness (Turcotte & Schubert, 1982). In Eqn. 1, V_i, the applied load of the i^{th} block is calculated as

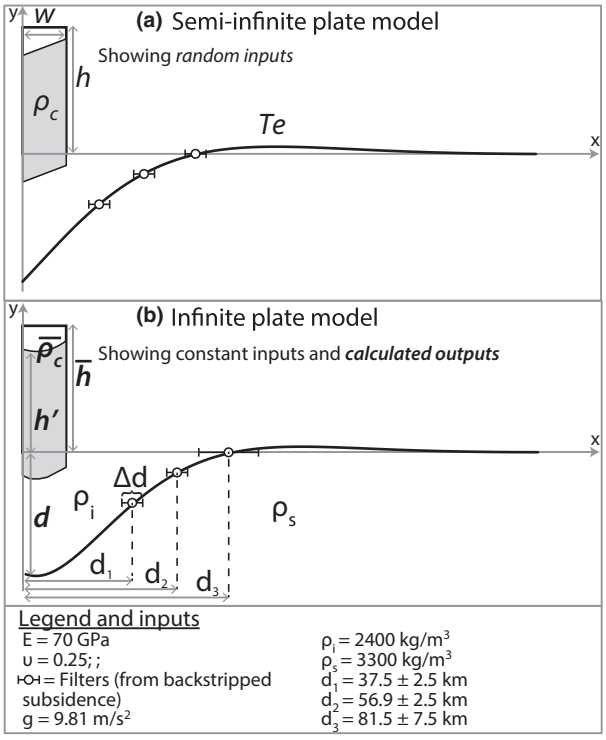

Fig. 2. Flexure model set up and key parameters. (a) Semi-infinite (broken) plate model and random variables. (b) Infinite (unbroken) plate model showing constant and calculated variables.

$$V_i = \rho_{ci}\; g\; h_i\; (x_{i+1} - x_i), \tag{3}$$

where ρ_{ci} is load density, h_i is the height and $(x_{i+1}-x_i)$ is the width of i^{th} block. In Eqn. 1, $f(u)$ is calculated as

$$f(u) = e^{-u}(\cos u + \sin u), \tag{4}$$

where

$$u = |x - c_i|\alpha^{-1} \tag{5}$$

and c_i is the position of the centre of the i^{th} load block.

The semi-infinite lithosphere model incorporates equations from Hetenyi (1979). Like the infinite plate, deflection is calculated as the cumulative effect of multiple topographic loads. The deflection at each individual point is then the sum of the deflections due to N applied loads calculated as

$$w(x) = \sum_{i=1}^{N} w_i(x), \tag{6}$$

where $w_i(x)$ is calculated by Hetenyi (1979; equation 23a) as

$$w_i(x) = \frac{V_i}{2\; g\; \Delta\rho\; \alpha}(C+2D)A - 2(C+D)B + E. \tag{7}$$

Terms A–E in Eqn. 7 are calculated by Hetenyi (1979; chapter 2.1, equation h) as follows:

$$A = e^{-\frac{x}{\alpha}}\left(\cos\frac{x}{\alpha} + \sin\frac{x}{\alpha}\right), \tag{8}$$

$$B = e^{-\frac{x}{\alpha}}\left(\sin\frac{x}{\alpha}\right), \tag{9}$$

$$C = e^{-\frac{c_i}{\alpha}}\left(\cos\frac{c_i}{\alpha} - \sin\frac{c_i}{\alpha}\right), \tag{10}$$

$$D = e^{-\frac{c_i}{\alpha}}\left(\cos\frac{c_i}{\alpha}\right), \tag{11}$$

and

$$E = e^{-\frac{|c_i - x|}{\alpha}}\left(\cos\frac{|c_i - x|}{\alpha} + \sin\frac{|c_i - x|}{\alpha}\right). \tag{12}$$

Young's Modulus, Poisson's ratio and gravitational acceleration were held constant at 70 Gpa, 0.25 and 9.81 m s^{-2}, respectively, for all model simulations. Load height randomly varied between 0.01 and 5 km. Load width ranged from 5 to 12.5 km for models which loaded the Linxia Basin lithosphere with half of the topographic load of the Jishi Shan or 10–25 km for models that loaded the Linxia Basin with the full Jishi Shan load. Effective elastic thickness (Te) was randomly assigned from 5 to 30 km. Load density (ρ_c) was assigned randomly between 2450 and 2850 kg m^{-3}. Density difference ($\Delta\rho = \rho_s - \rho_i$) was set at 900 kg m^{-3} assuming an average density for asthenosphere of 3300 kg m^{-3} and a density of basin-filling sedimentary rocks of 2400 kg m^{-3}. The position of the load block was pinned at the west side of the Jishi Shan (Fig. 3). Each model run generated 100 000 random flexural profiles which were then filtered to accept those that produced the observed subsidence at the location of the measured sections at 13.1, 7.6, 6, 4.5 and 2.6 Ma. We accounted for the fact sediment loading adds to the mass of the tectonic load using Eqn. 13 (below, and Fig. 4),

$$h' = \bar{h} - d\left[1 - \left(\frac{\rho_i}{\bar{\rho}_c}\right)\right], \tag{13}$$

where $\bar{h}$ is the mean height of the modelled load block, d is the subsidence at the centre of the load block and ρ_i and $\bar{\rho}_c$ are the assigned infill density and mean load density, respectively. Conceptually, this approach decreases the area of the basin infill beneath the tectonic load so that its density matches the density of the tectonic load. The resultant decrease in height of the infilling material was subtracted from the height of the tectonic load block to obtain the final topographic elevation. This is equivalent to the more common approach of modelling basin infill as additional load blocks (Jordan, 1981; Yong *et al.*, 2003; Fosdick *et al.*, 2014), but is less computationally intensive (Fig. 4).

Flexural profiles were filtered using the calculated decompacted sediment thickness at two locations, and a third location which was treated as the distal edge of the foredeep. The two stratigraphic sections used included Wangjiashan and Maogou (Fig. 1b). At each of these locations we placed an uncertainty window (Δd, Fig. 2) of 5 km and accepted subsidence profiles which passed within the uncertainty window. The basin zero edge was taken at the edge of Cenozoic deposition within the

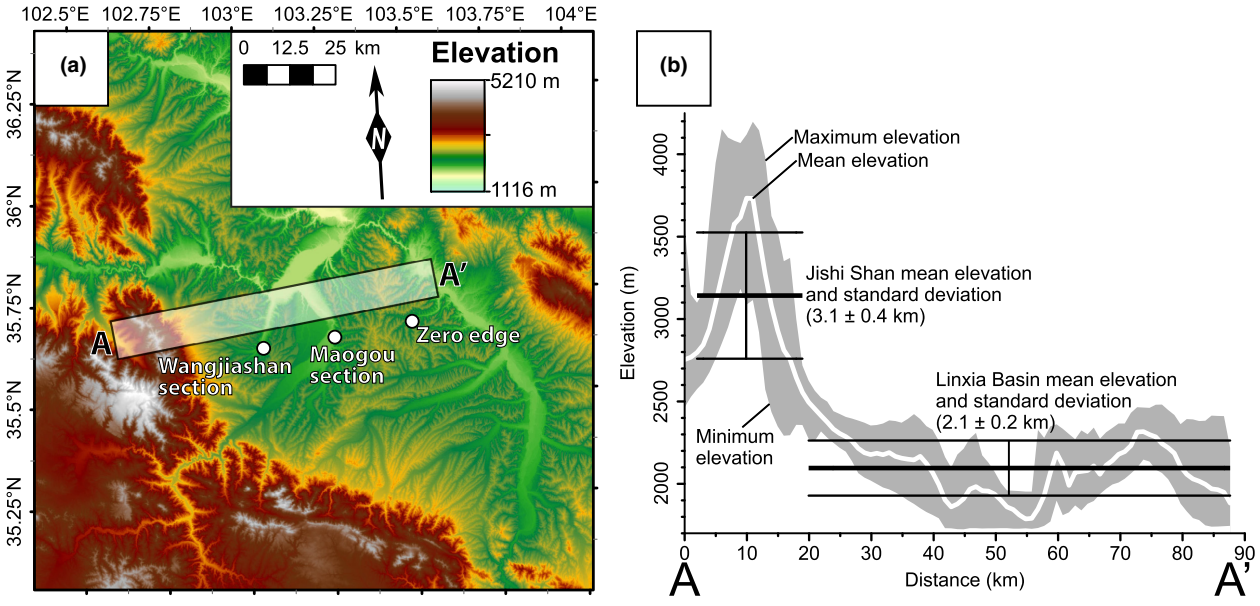

Fig. 3. (a) Digital elevation model of the Linxia Basin showing the three control points used to filter subsidence profiles and the 10-km-wide swath profile. (b) Swath profile showing minimum, mean, and maximum elevations. Also shows the mean elevation for the Jishi Shan and Linxia Basin and the x-interval over which the means are calculated.

basin (35.6796875° N, 103.5083° E, Fig. 1b) (CGIR-CUG, 2006a,b). The uncertainty window on the zero-edge location was set at 15 km and has minimal impact on the accepted flexural profiles. Formation ages are based on both biostratigraphic and magnetostratigraphic dates (Qiu & Qiu, 1990; Qiu *et al.*, 1990, 2002; Gu *et al.*, 1995a,b; Fang *et al.*, 1997, 2003; Deng *et al.*, 2013). The chronology for and Wangjishan section between 12 and 29 Ma is based on lithostratigraphic correlation with the Maogou section rather than on magnetostratigraphy from the section itself (Fang *et al.*, 2003). Recognizing the need for independent constraints on basin chronology, we utilize the chronology of Fang *et al.* (2003) due to the coincidence between enhanced subsidence episodes and changes in sediment provenance observed in the basin fill and independently observed tectonic episodes when using this chronology. Figure S1 presents basin subsidence profiles using the chronology of Deng *et al.* (2013).

We focus on five dated horizons which post-date the onset of exhumation in the Jishi Shan as well as post-dating the cessation of exhumation in the West Qinling and Laji Shan: 2.6, 4.5, 6, 7.6 and 13.1 Ma (Clark *et al.*, 2010; Lease *et al.*, 2011, 2012a). Magnetostratigraphy provides independent constraints on chronology for each of the sections in question for this time interval. In this work, the Hujialiang Formation is included in the Dongxiang Formation because the magnetostratigraphic chronology was developed prior to the formation's recognition (Fang *et al.*, 2003). Each of these time slices was filtered for the cumulative tectonic subsidence since 14 Ma at the three locations.

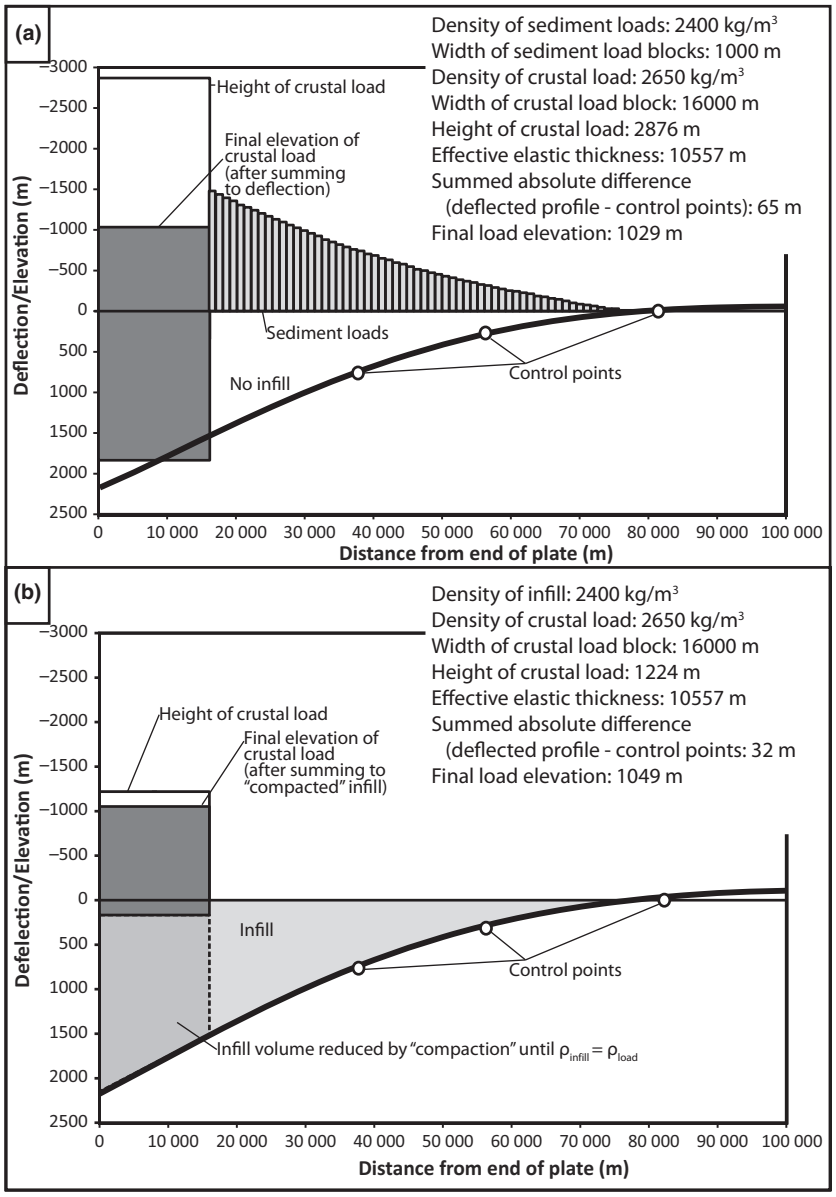

Fig. 4. Comparison of flexural models where the basin-filling sediment load is modelled either as (a) a tapered series of load blocks or (b) as filling the space created by the deflected plate. Both profiles were created by minimizing the summed absolute difference between the deflected plate and the three control points and result in final load elevations that are within 2% of each other.

Model calibration was conducted by comparing the modelled 2.6 Ma subsidence profile and associated topography under a number of different model parameters to the observed modern topography in the Jishi Shan. For the initial calibration we considered both a semi-infinite and infinite plate, as well as considering subsidence due to the full width of the Jishi Shan topography versus loading by the Jishi Shan half-width. Model results were

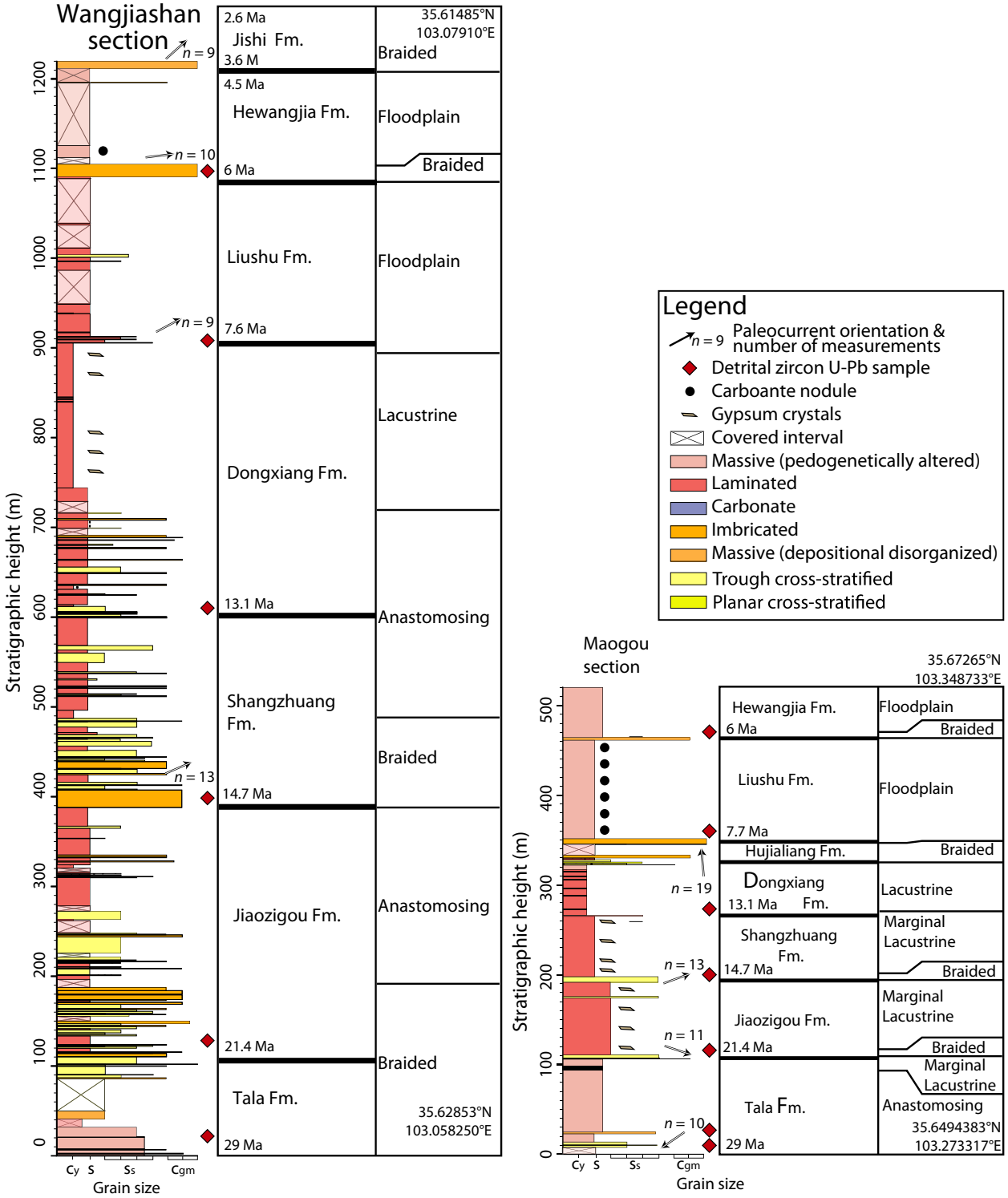

Fig. 5. Stratigraphic sections for the Wangjiashan and Maogou locations. See Fig. 1 for locations.

compared to observed modern mean topographic relief across the Jishi Shan to determine which combination of factors best reproduces the modern observations. A mean difference in elevation of 1.0 ± 0.4 km (1σ) was calculated between mean Jishi Shan elevations (3.1 ± 0.4 km, 1σ) and the mean elevation of the Linxia Basin (2.1 ± 0.2 km, 1σ) along a 10-km-wide swath (Fig. 3). The model which best reproduced the observed modern elevation difference was then used for each preceding time step.

RESULTS

Measured stratigraphic sections

The greatest thickness of Cenozoic stratigraphy of the Linxia Basin is at least 1.2 km, located in the western portion of the basin adjacent to the Jishi Shan. Strata thin eastward to at least 500 m at the Maogou section, the middle of the basin (Fig. 5; Fang *et al.*, 2003). There is an overall upward-fining trend from the Oligocene Tala Formation through the top of the middle–late Miocene Dongxiang Formation. This is followed by a minor upward-coarsening trend through the end of the Pliocene. Basin strata are dominated by mudstone with subordinate sandstone and conglomerate beds.

Both the Wangjiashan and Maogou sections display two maxima in sediment accumulation rates: the first in the middle Miocene and the second in the late Miocene (Fig. 6 and Table S6). Both sections show minimal Paleogene sediment accumulation. Decompacted sediment accumulation rates in the Wangjiashan section increase from ≤17 m Myr^{-1} prior to 21.4 Ma to an average of *ca.* 50 m Myr^{-1} between 21.4 and 14.7 Ma. However, this early Miocene increase in the Wangjiashan section is not mirrored by a similar increase in the Maogou section. There is an approximately threefold increase in sediment accumulation rates at both the Wangjiashan and Maogou locations between 14.7 and 13.1 Ma. Sediment accumulation rates return to early Miocene values in both locations from 13.1 to 7.6 Ma, before increasing again between 7.6 and 6 Ma. Sediment accumulation rates begin to tail off after 6 Ma, and, by Pliocene time, the sediment accumulation rates are essentially zero.

Zircon U-Pb geochronology

A total of 2266 new zircon ages from 12 samples are reported here (Table S3 and S4). We combine our samples with samples from published sources (Lease *et al.*, 2007, 2012a; Weislogel *et al.*, 2010) for plotting as probability density plots (PDPs). The PDPs show each age and its uncertainty as a normal distribution, and sum all ages from a sample into a single curve (Figs 7, 8 and 9).

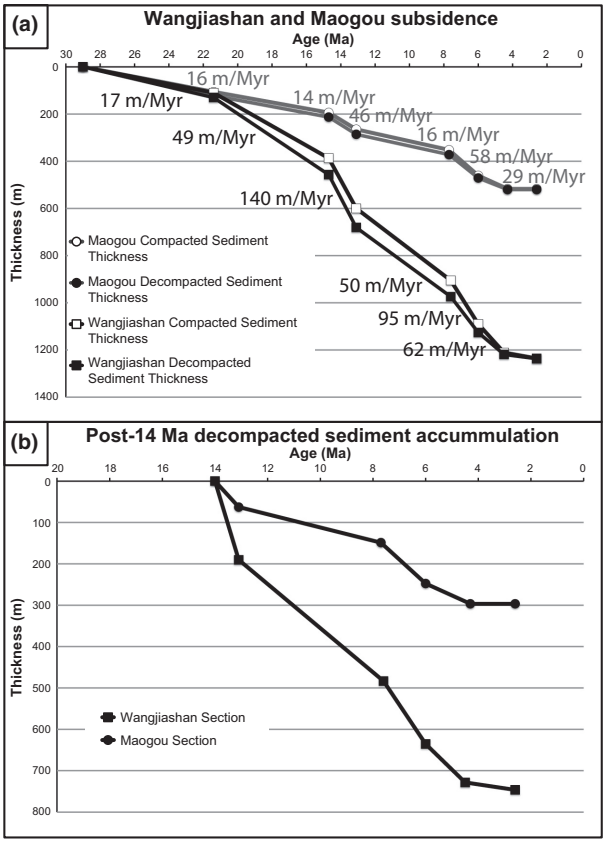

Fig. 6. (a) Cumulative compacted and decompacted sediment accumulation curves for the Wangjiashan and Maogou locations since 29 Ma. (b) Cumulative compacted and decompacted sediment accumulation curves for the Wangjiashan and Maogou locations since 14 Ma. Post-14 Ma subsidence is attributed primarily to flexural loading due to exhumation and uplift of the Jishi Shan and is used in flexural modelling.

Potential sediment source samples' zircon U-Pb age spectra are dominated by peaks between 200–300, 400–500, 1700–2100, and 2300–2600 Ma ranges. Potential sediment sources including the Cretaceous sandstone and Jishi Shan are dominated by early Paleozoic zircons. The northern sources, including samples from the Laji Shan, Maxian Shan and Riyue Shan, are also dominated by early Paleozoic zircon ages but include minor age modes in the Permo-Triassic and Paleoproterozoic. The West Qinling to the south of the Linxia Basin includes very narrow peaks with a dominant Permo-Triassic mode, a secondary early Paleozoic age mode, and very minor additions of Paleoproterozoic ages. Finally, Triassic strata of the northeast depocenter of the Songpan-Ganzi complex (hereafter referred to as the Songpan-Ganzi source) exposed in the West Qinling and farther south features three sub-equal broad peaks slightly overlapping Permo-Triassic and early Paleozoic age modes and a 1700–2100 Ma Paleoproterozoic peak. This source also has a fourth major Neoarchean–Paleoproterozoic peak between

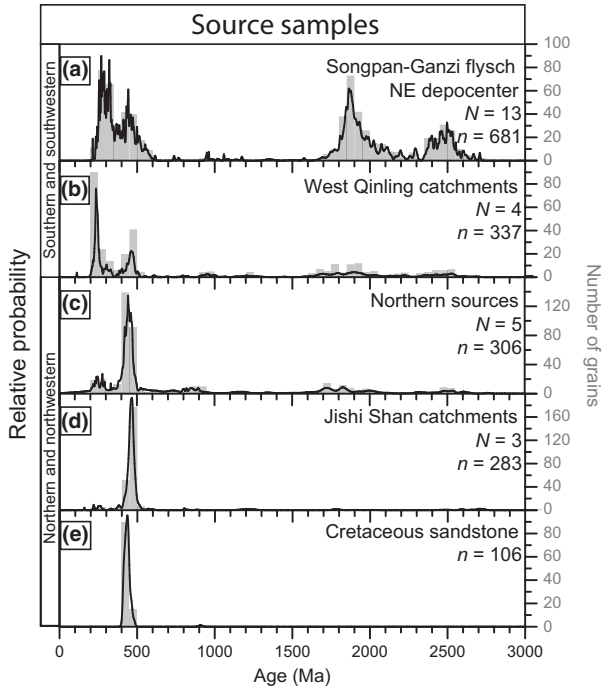

Fig. 7. Probability density plots and histograms for source samples. Includes data from this study, as well as from Weislogel *et al.* (2010) and Lease *et al.* (2007). See Table S1 for details of samples included in each source.

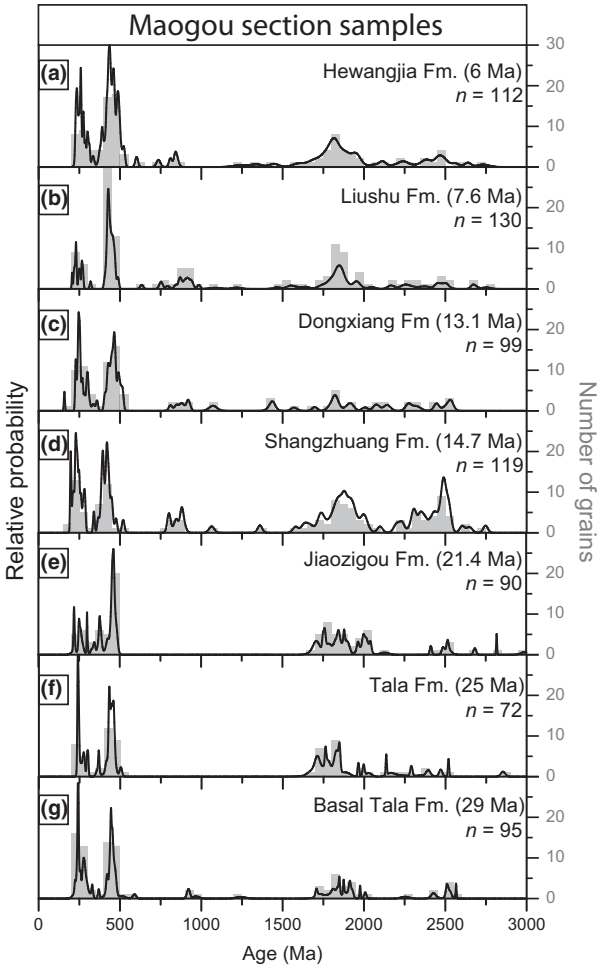

Fig. 8. Probability density plots and histograms for Maogou section samples. See Table S1 for details of samples included here.

2300 and 2600 Ma comprised of slightly lower proportion of grain ages.

Multidimensional scaling shows a systematic variation between southern sources versus northern/eastern sources (Figs 10 and 11 and Table S5). In the Wangjiashan section there is a systematic increase in similarity between basin samples and southern sources between 29 Ma and 14.5 Ma seen in both the Cross-correlation coefficient and the Kuiper V value. Similarly, in the Maogou section, there is an increase in similarity between detrital zircon age spectra from basin sediments and southern sources, particularly between 21 Ma and 14.5 Ma (Fig. 10). Between 14.5 Ma and 13.1 Ma, there is an abrupt increase in the similarity to northern/northwestern sources and the basin samples at both locations coincident with the onset of exhumation in the Jishi Shan. At the Wangjiashan location, samples continue to decrease in similarity with Songpan-Ganzi as well as West Qinling sources through the late Miocene while continuing to become more similar to northern and eastern sources; particularly, the Cretaceous sandstone and Northern Sources. However, this trend is not seen at the Maogou location. Here, the similarity between basin and northern/northwestern source samples does not increase after 7.5 Ma. Instead the 6 Ma sample reflects a mixture of all potential sediment sources.

Flexural modelling

The calibrated flexural model successfully reproduced observed topography using a broken plate loaded with the full load width of the Jishi Shan (Fig. 12 and Table S7). Modelled relief using these parameters was 1.3 ± 0.3 km (1σ). We model the 13, 7.6, 6 and 4.5 Ma time slices using a broken plate loaded with the full load of the Jishi Shan. Average effective elastic thickness for these models was 10.5 ± 0.5 km. This is comparable to estimates of 10–20 km calculated from remotely sensed geophysical data (Braitenberg *et al.*, 2003; Jordan & Watts, 2005; Deng *et al.*, 2014; Chen *et al.*, 2015). In comparison, models involving half the load width of the Jishi Shan or an infinite plate both produce excess topographic relief. The broken plate model loaded with half of the load width of the Jishi Shan yielded an overestimate of relief (2.6 ± 0.7 km), but

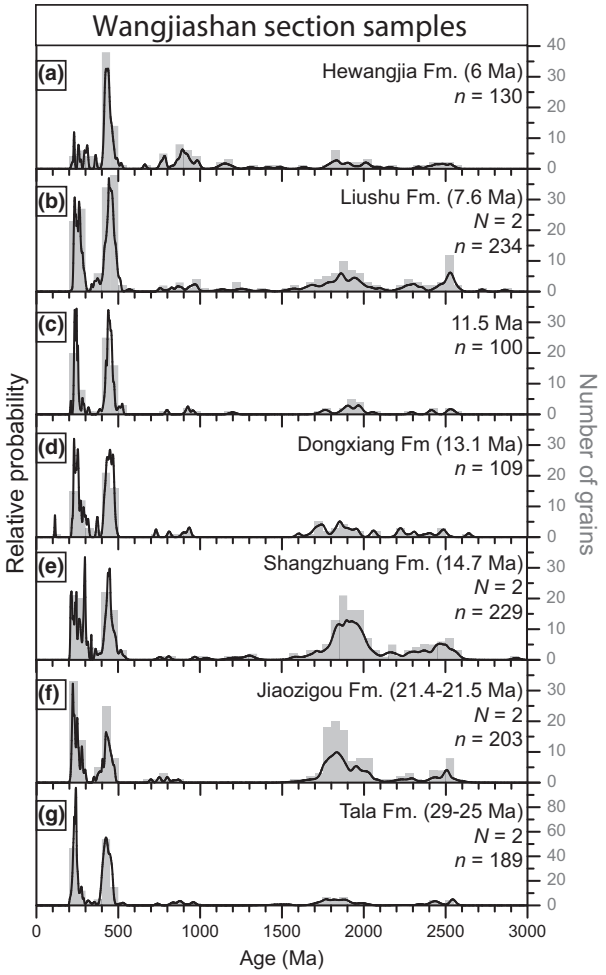

Fig. 9. Probability density plots and histograms for Wangjiashan section samples. Includes data from this study, as well as from Lease *et al.* (2012a). See Table S1 for details of samples included here.

yielded an acceptable elastic thickness of 12.0 ± 0.9 km. Models involving an infinite plate loaded with the full width of the Jishi Shan produce 1.9 ± 0.6 km of relief with an unacceptably low elastic thickness of 7.0 ± 0.6 km.

Flexural models are constrained by sediment accumulation histories and hence pulses of relief generated by flexural modelling of time slices at 13, 7.6, 6 and 4.5 Ma mirror the pulses of sediment accumulation observed in the subsidence profiles. The surface uplift rate was 0.31 ± 0.06 mm yr^{-1} from 14 to 13 Ma. From 13 to 7.6 Ma surface uplift rates decrease by more than half to rates of 0.09 ± 0.04 mm yr^{-1}, before accelerating again to 0.16 ± 0.25 mm yr^{-1} between 7.6 and 6 Ma. After 6 Ma, surface uplift rates tail off progressively and reach uplift rates of zero between 4.5 and 2.6 Ma. By 4.5 Ma, relief is greater than, although within uncertainty of, the modern. In contrast to the continuous increase in relief, the effective elastic thickness and width of the Jishi Shan load do not change systematically with time and have means of 10.5 ± 0.5 km (1σ) and 16.8 ± 0.2 km (1σ), respectively. As with all inverse problems, this set of solutions is nonunique. Therefore, below we compare the results of our flexural model to the detrital zircon and stable isotope records from the Linxia and Xunhua basins.

INTERPRETATION

Zircon U-Pb geochronology

We attribute the increase in similarity between basin samples and southern (West Qinling and Songpan-Ganzi) sources between 29 and 21.4 Ma to erosion of this highland following the Eocene onset of exhumation (Clark *et al.*, 2010). Following exhumation of the Laji Shan at *ca.* 22 Ma (Lease *et al.*, 2011; Duvall *et al.*, 2013) and cut-off of potential northward sediment dispersal systems, sediment would have been routed axially from the Xunhua Basin in the west eastward towards the Linxia Basin, following the approximate course of the modern Yellow River. This sediment load would have included sediment shed from the Laji Shan to the north but also contained an admixture of southern sources, characterized by zircons with U-Pb ages >1700 Ma. The decrease in similarity between basin samples and southern sources between 14.7 Ma and 13.1 Ma reflects the cut-off of this source due to the onset of exhumation in the Jishi Shan (Lease *et al.*, 2011, 2012a). Currently, only short, steep drainages flow from the West Qinling to Linxia Basin and hence do not integrate the broad Paleoproterozoic range of zircon ages present in the Songpan-Ganzi (Figs 1b and 7).

Reintroduction of the >1700 Ma age peak at 7.6 Ma at the Maogou location and its strengthening by 6 Ma may represent either dissection of the Jishi Shan to the west and reestablishment of the paleo-Yellow River course, or direct sourcing of sediment from the West Qinling to the south. We favour the former interpretation because eastward oriented paleocurrent indicators in this interval (Fig. 5) implicate a source to the west. In addition, the last major tectonic activity in the West Qinling occurred at 45–50 Ma (Clark *et al.*, 2010). Major changes in drainage organization in the recently exhumed Jishi Shan present a more plausible explanation for the changes in Linxia Basin than a similar reorganization in the West Qingling >35 Myr after tectonic activity in that range. Permo-Triassic plutons are primarily exposed west of the Wangjiashan section (south of Xunhua Basin, Fig. 1b) while both Permo-Triassic and Paleoproterozoic zircons are present in the Songpan-Ganzi sedimentary rocks (Fig. 9a). The

detrital zircon ages from the Maogou section suggest an increasing southern/southwestern contribution after 13.1 Ma, first with the increase in *ca.* 1700 Ma zircons at 7.6 Ma and then with the increase in both Permo-Triassic and Paleoproterzoic zircons at 6 Ma (Fig. 10a–c). This is mirrored by an increase in the southwestern source in the Wangjiashan section through 7.6 Ma (Fig. 11b). However, that trend is reversed in the Wangjiashan section between 7.6 and 6 Ma, when the relative abundance of both Permo-Triassic and *ca.* 1700 Ma zircons decrease (Fig. 11a–b). Where data are available from the Xunhua Basin between 19 and 10 Ma, the proportions of Permo-Triassic and >1700 Ma grains do not significantly vary in the Hualong section (Lease *et al.*, 2012a), suggesting that the Xunhua Basin was not cut-off from the southern source during the Neogene as was the Linxia Basin. We interpret the diminished proportion of >1700 Ma grains at the Wangjiashan location after 7.6 Ma as a result of being off-axis relative to the now entrenched integrated sediment dispersal system cutting through the uplifted Jishi Shan. Sediments at the Wangjiashan location are dominantly locally sourced from the windward (eastern) side of the Jishi Shan.

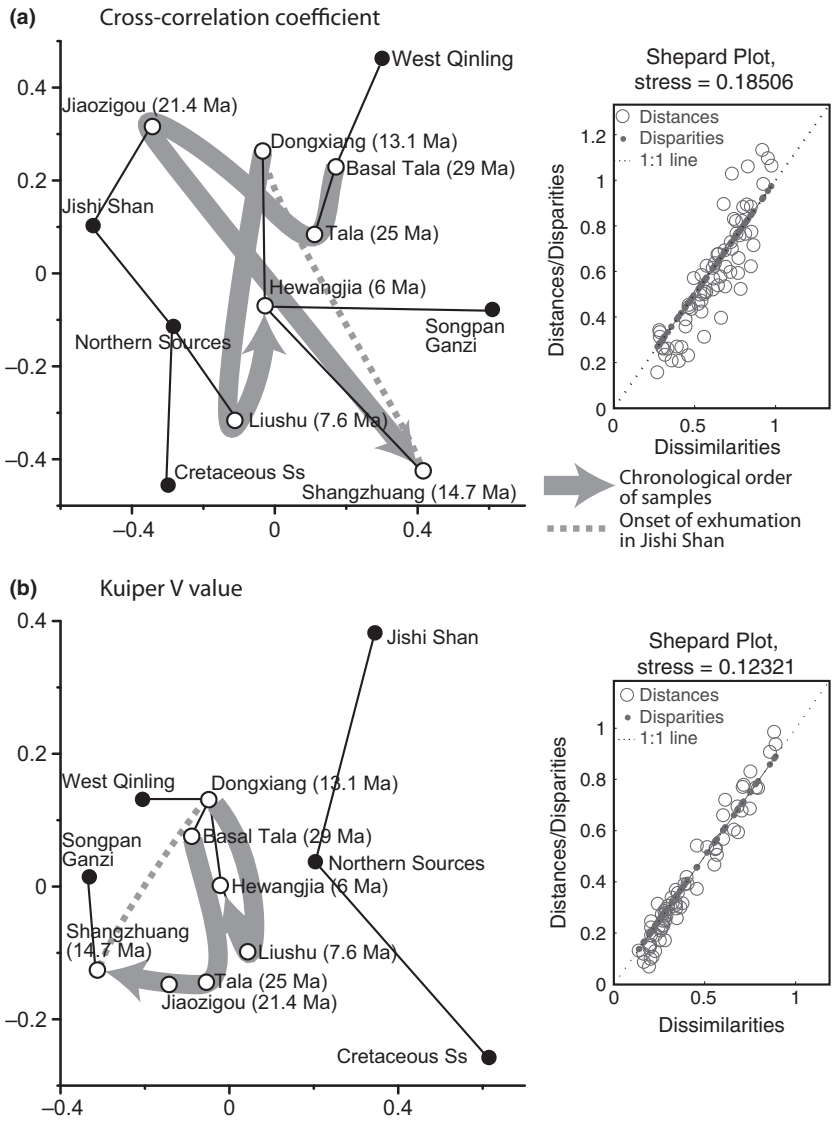

Fig. 10. Two-dimensional multidimensional scaling plot of the source and Maogou section samples. Dissimilarity is based on (a) the complement of the Cross-correlation coefficient or (b) the Kuiper V value. Both metrics show increased similarity between basin samples and southern (Songpan-Ganzi) sources between 29 and 14.7 Ma, followed by an abrupt increase in similarity to northern sources between 14.7 and 13.1 Ma. The late Miocene samples become marginally more similar to southern sources, likely reflecting a well-mixed source area.

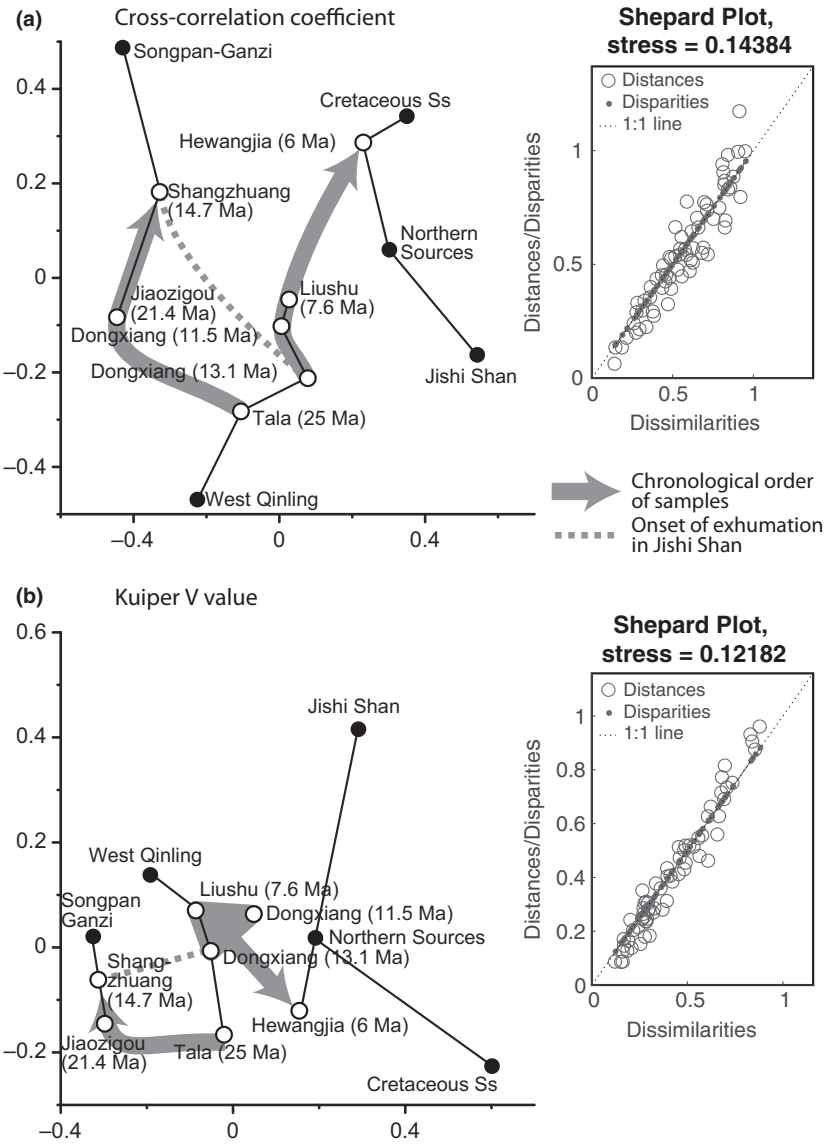

Fig. 11. Two-dimensional multidimensional scaling plot of the source and Wangjiashan section samples. Dissimilarity is based on (a) the complement of the Cross-correlation coefficient or (b) the Kuiper V value. Both metrics show increased similarity between basin samples and southern (Songpan-Ganzi) sources between 29 and 14.7 Ma, followed by an abrupt increase in similarity to northern sources between 14.7 and 13.1 Ma. The late Miocene samples become more similar to northern/northwestern sources, likely reflecting continued dominance of the Jishi Shan as a source for this location.

Subsidence analysis

We attribute the increase in sediment accumulation and subsidence rate in the Wangjiashan section at *ca*. 21.4 Ma to the onset of exhumation in the Laji Shan possibly in combination with resumed exhumation in the West Qinling (Clark *et al.*, 2010; Lease *et al.*, 2011). Although thermochronology results point to early Miocene exhumation of the Maxian Shan (Duvall *et al.*, 2013), the increase in sediment accumulation rates at 21.4 Ma is not observed in the nearby Maogou section. Furthermore, the basin fill thins from the Maogou location towards the Maxian Shan (i.e. towards the modelled zero edge). The absence of a basin response to early Miocene exhumation suggests that the Laji Shan was the primary subsidence driver, but that the flexural effect of exhumation of loading by the Laji Shan was attenuated in the Maogou location and only affected proximal locations. Exhumation of the Maxian Shan appears to have had little effect on sediment accumulation rates in Linxia Basin.

The Laji Shan experienced rapid cooling initially, followed by slow cooling after 18 Ma (Lease *et al.*, 2011), suggesting that while exhumation of the Laji Shan influenced basin subsidence, it was not the primary driver in the middle Miocene. We attribute the middle Miocene increase in sediment accumulation, which is observed in

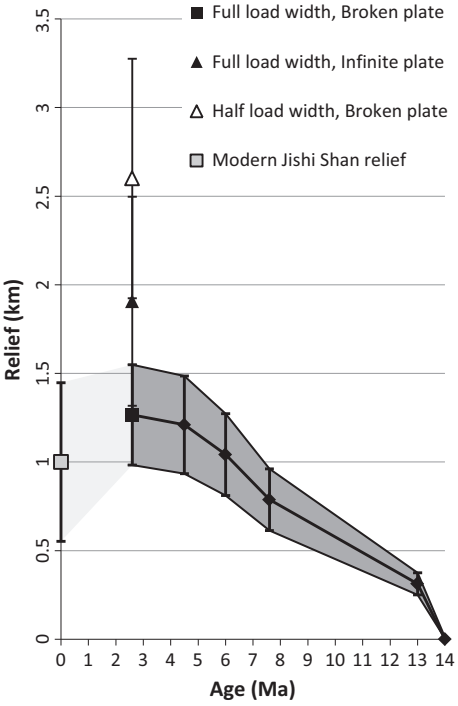

Fig. 12. Comparison of the final load elevation from flexural modelling and modern relief in the Jishi Shan. Models with either a half load width or infinite (unbroken) plate overestimate the relief generated for the 2.6 Ma step. The full load with a semi-infinite (broken) plate model best reproduces modern relief and is used as the basis for modelling relief generation through time.

the Wangjiashan and Maogou sections and also in Xunhua Basin to a pulse of exhumation in the Jishi Shan that began at *ca*. 14 Ma (Lease *et al.*, 2011, 2012a). The subsequent decrease in sediment accumulation rates, also observed at both the Wangjiashan and Maogou locations, suggests that the rate of topographic growth in the Jishi Shan may have decreased between 13.1 and 7.7 Ma. If accurate, this complements thermochronological evidence for continued rapid exhumation of the Jishi Shan between *ca*. 14–13 Ma and *ca*. 6 Ma (Lease *et al.*, 2011) and suggests that increased erosion may have offset rock uplift in the late Miocene. The increase in sediment accumulation rates at *ca*. 7.6 Ma is coincident with additional tectonic activity in the region including an interpreted 10° degree clockwise rotation of the Linxia Basin (Fang *et al.*, 2003) and also with eastward propagation of the Kunlun and Haiyuan faults and incorporation of the Linxia region into the Kunlun-Haiyuan transpressional corridor (Duvall *et al.*, 2013).

DISCUSSION

Development of relief and rainshadows

Development of relief can drive divergence in precipitation amount, $\delta^{18}O$ values of precipitation ($\delta^{18}O_p$ values) and aridity on the windward and lee sides of the developing mountain range. Divergence in the isotopic record of previously contiguous basins can therefore be used to track the timing of surface uplift of basin-dissecting ranges (Kleinert and Strecker, 2001; Hough *et al.*, 2011). Cooling and adiabatic expansion of water vapour leads to isotope fractionation between the liquid and vapour phases while vapour ascends the windward side of a mountain range, causing a decrease in the $\delta^{18}O$ values of precipitation ($\delta^{18}O_p$ values; Dansgaard, 1964; Rozanski *et al.*, 1993; Rowley, 2007). Relief can also produce a decrease in $\delta^{18}O_p$ values on the windward side of

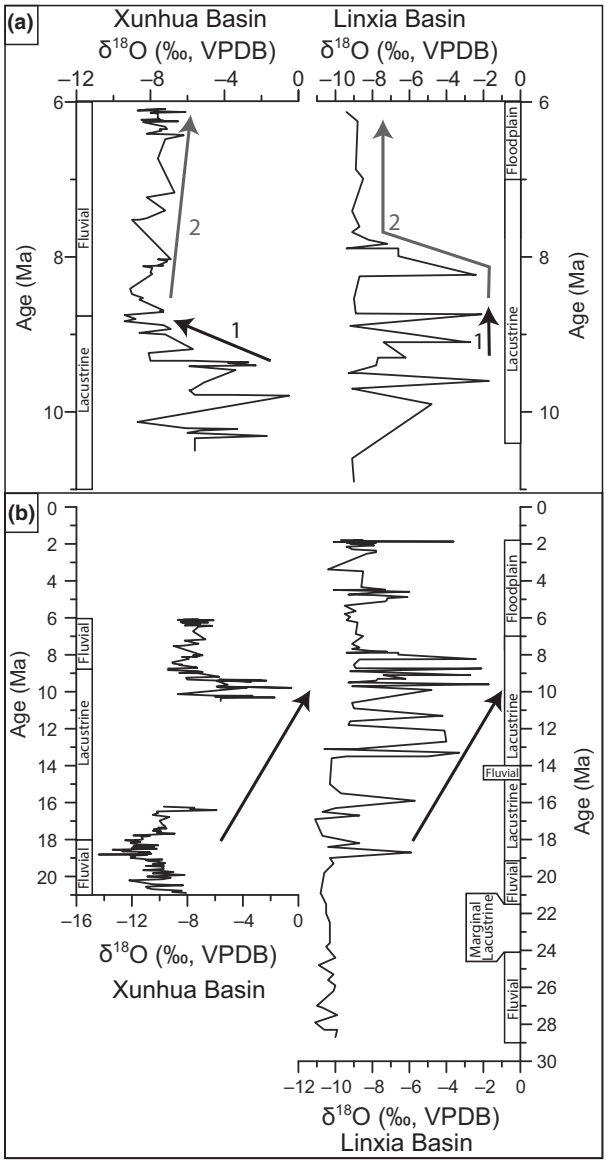

Fig. 13. Oxygen isotopic data for the Linxia and Xunhua basins. (a) Shows the two post-9.3 Ma divergent trends in $\delta^{18}O$ values. (b) Shows the pre-9.3 Ma lock-step evolution of the two stable isotope records. Data are from Hough *et al.* (2014) and Dettman *et al.* (2003).

mountain ranges by an increase in the absolute precipitation amount (the "amount effect": e.g. Vuille *et al.*, 2003, 2005). Rainout of water vapour in the windward side results in development of an arid rainshadow on the lee side of the mountain range. A decrease in relative humidity following topography-induced changes in atmospheric circulation may cause an increase in $\delta^{18}O_p$ values due to subcloud evaporation and in surface waters due to evaporative enrichment of ^{18}O (Bershaw *et al.*, 2012, 2016).

Divergence in stable isotope data (compiled from Dettman *et al.* (2003) and Hough *et al.* (2014)) and depositional environments between the Xunhua and Linxia basins provide evidence for hydrological separation of these two basins followed by development of a rainshadow in the Xunhua Basin. In both basins, the minimum, mean, and maximum $\delta^{18}O$ values of paleosol and lacustrine carbonates ($\delta^{18}O_c$ values) increase from 18–19 Ma to *ca.* 9.3 Ma (Fig. 13). There is a gap in the stable isotopic record in the Xunhua Basin from 16.22 to 10.5 Ma. However, following the hiatus, between 10.5 and 9.3 Ma, the Xunhua and Linxia sections share similar most-negative $\delta^{18}O_c$ values (−8.7 and −9.3 ‰, respectively, Fig. 13). Furthermore, ANOVA analysis indicates that the mean $\delta^{18}O_c$ values from the two data sets between 10.5 and 9.3 Ma cannot be discriminated at the >95% confidence level using a standard t test (mean and variance of -4.8 ± 3.8 ‰ and -7.0 ± 7.7 ‰, for Xunhua and Linxia basins, respectively, $t(8) = 1.97$, $p = 0.08$). Following previous studies, we interpret these changes as responding to regional climate changes (e.g. Dettman *et al.*, 2003).

Following 9.3 Ma, the stable isotope records in the Xunhua and Linxia basins show two divergent trends possibly correlated the growth of Jishi Shan topography. The initial divergence occurs at *ca.* 9 Ma when $\delta^{18}O_c$ values in the Xunhua Basin decrease to minimum values of −9.4 ‰ (mean for 9–8.75 Ma = −8.4 ‰). Over the same interval mean $\delta^{18}O_c$ values in the Linxia Basin remain unchanged. The second divergent trend between the two basins marked by an increase in mean $\delta^{18}O_c$ values in the Xunhua Basin and decreasing mean and invariant minimum $\delta^{18}O_c$ values in the Linxia Basin. After 8.83 Ma paleosol carbonate $\delta^{18}O_c$ values in the Xunhua Basin increase at a rate of 0.28 ‰/Myr. Mean $\delta^{18}O_c$ values for the final 0.5 Myr where the basins share records (6.5–6.0 Ma) are −7.5 ‰: 0.9 ‰ higher than when the increasing trend began (9–8.75 Ma). This trend is robust, with samples from the final 0.5 Myr being differentiable from the first 0.5 Myr at the 95% confidence level based on a t test (mean and variance of -8.3 ± 0.8 ‰ and -7.4 ± 0.4 ‰, for the beginning and ends, respectively, $t(10) = 2.22$, $p = 0.04$). In contrast to this record, maximum and mean $\delta^{18}O_c$ values from the Linxia Basin decrease abruptly at *ca.* 8 Ma while minimum values remain unchanged. The $\delta^{18}O_c$ values in the Linxia Basin subsequently remain low and show no trend through 6 Ma (range = −7.2 to −9.4 ‰).

In the modern system, there is a 1.2 ‰ difference in the $\delta^{18}O$ values of summer (May–September) precipitation in the Linxia and Xunhua basins (Hough *et al.*, 2011). Barring a significant change in the seasonality of precipitation or carbonate formation, the 0.9 ‰ increase in paleosol $\delta^{18}O_c$ values between 8.83 and 6 Ma in the Xunhua Basin is consistent with development of 75% of the modern rainshadow effect across the Jishi Shan. Furthermore, the increase in carbonate $\delta^{18}O_c$ values in the Xunhua Basin corresponds to rapid topographic growth in the Jishi Shan between *ca.* 8.8 and 6 Ma (Fig. 12). However, the increase in $\delta^{18}O_c$ values does not linearly correlate with increasing calculated paleorelief, although quantification of the relationship between the rate of rainshadow development and topographic development is beyond the scope of this work. In making this interpretation, we note that the observed 0.9‰ increase in the carbonate $\delta^{18}O_c$ values, although statistically robust, may be the result of incomplete sampling of an extremely noisy record and that the modern stable isotope record to which it is compared was collected over *ca.* 1.5 years (Hough *et al.*, 2011).

Relief generation and basin evolution

Changes in the provenance, stable isotopic, sediment accumulation history, and flexural model results link the exhumation and topographic evolution of the Jishi Shan. At *ca.* 22 Ma, prior to the onset of Jishi Shan exhumation, exhumation of the Laji Shan cut-off northward sediment dispersal systems (Fig. 14a). This resulted in rerouting of sediment dispersal systems axially from the Xunhua Basin in the west, eastward towards the Linxia Basin, following the approximate course of the modern Yellow River (Hough *et al.*, 2014). Geochronological analysis of detrital zircons from the modern Yellow River above Linxia shows a prominent age mode between 1500 and 2100 Ma (Nie *et al.*, 2015). Axial routing of these southern-sourced sediment dispersal systems accounts for the increase in proportion of zircons with U-Pb ages >1700 Ma between 29 and 14.5 Ma (Figs 8 and 9). It also accounts for the increase in similarity between basin samples and the Songpan-Gonzi flysch compilation (Figs 7, 10 and 11).

The increase in similarity with northern and northwestern sources between 14.7 Ma and 13.1 Ma reflects the cut-off of the southern source and enhancement of contributions from northern and northeastern sources due to the onset of exhumation in the Jishi Shan (Lease *et al.*, 2011). However, the stable isotopic record in both basins trends towards more positive $\delta^{18}O_c$ values suggesting that both basins were dominated by a similar climate regime. Flexural modelling indicates development of

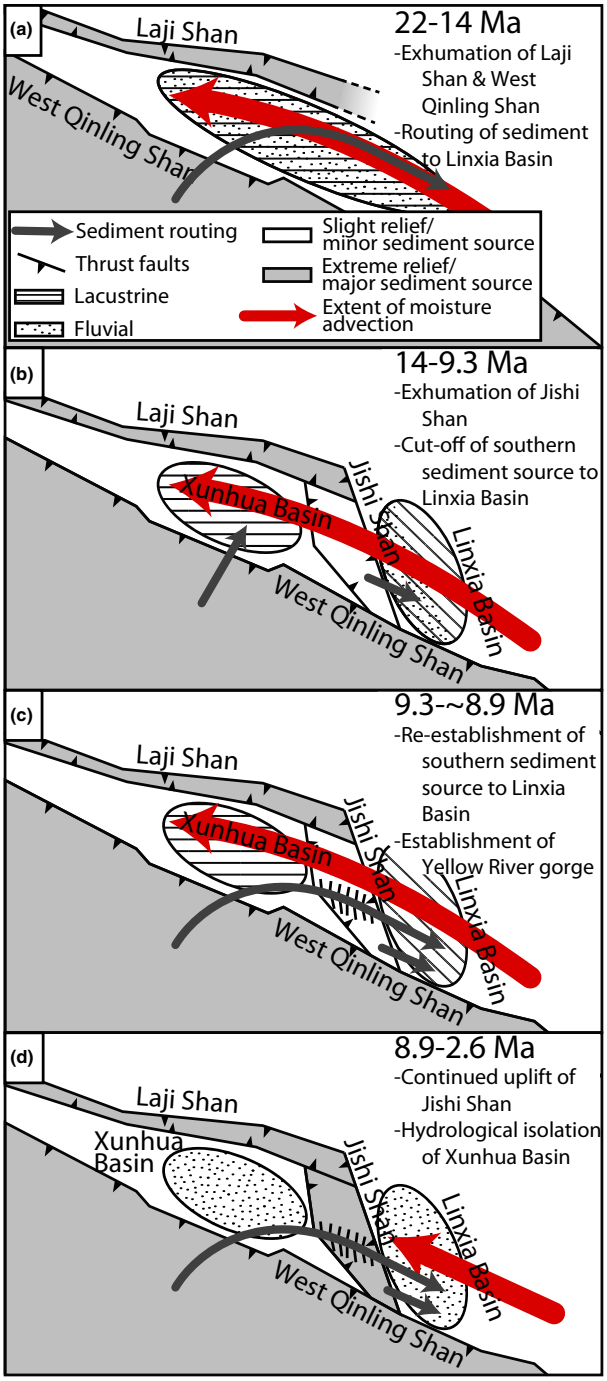

Fig. 14. Schematic paleogeographic maps showing the Neogene evolution of the Linxia and Xunhua basin pair.

minor relief (0.3 ± 0.1 km) by 13 Ma suggesting that, although sufficient relief had been generated to disrupt and pond the fluvial systems, it was insufficient to intercept moisture-bearing airmasses.

Between the onset of exhumation of the Jishi Shan at 14 Ma and 9.3 Ma, the lacustrine systems of the Xunhua and Linxia basins experienced a similar evolution: effected by similar climate regimes (Fig. 14b). Decreasing $\delta^{18}O_c$ values and a change from lacustrine to fluvial depositional environments in the Xunhua Basin suggest a breaching of the Jishi Shan dam at 9.3 Ma. Prior to 9.3 Ma the Xunhua Basin was dammed, but hydrologically open as indicated by the scarcity of evaporite deposits and lack of correlation between $\delta^{18}O_c$ and $\delta^{13}C_c$ values during this time interval (Lease *et al.*, 2012a; Hough *et al.*, 2014). The transition to fluvial deposition in the basin is complete by at 8.8 Ma (Hough *et al.*, 2014). Following our preferred interpretation outlined above, reintroduction of the >1700 Ma age peak by 7.5 Ma at the Maogou and Wangjiashan locations points to upstream–downstream connectivity between the Xunhua and Linxia basins (Lease *et al.*, 2012a). The increase in this population by 6 Ma at Maogou, and its decrease at Wangjiashan likely represents reestablishment and entrenchment of the paleo-Yellow River course (Fig. 14c). This entrenchment resulted in bypass of sediment from the southern sources at the Wangjiashan location which becomes less similar to southern/southwestern sources after 7.6 Ma.

The end of lacustrine conditions in the Xunhua Basin and transition to fluvial conditions at 8.8 Ma is accompanied by an apparent increase in aridity in the basin. This aridity is not expressed in the Linxia Basin record as the lowest $\delta^{18}O$ values remain unchanged through this interval (Fig. 13), while that in Xunhua Basin shows a slight increase in $\delta^{18}O$ values. The synchronously increasing aridity on the leeward side of the Jishi Shan, and decrease in mean $\delta^{18}O$ values and stability in minimum $\delta^{18}O$ values in the Linxia Basin $\delta^{18}O$ record (e.g. Fan *et al.*, 2007) suggests that by 8 Ma the Jishi Shan achieved sufficient elevation to begin to intercept moisture-bearing airmasses, and that hydrologic separation occurred later than previously thought (Fig. 14d; Hough *et al.*, 2011, 2014).

Flexural modelling indicates that there was 0.8 ± 0.2 km of relief in the Jishi Shan by 8 Ma. This is consistent with the 1 km of relief needed to induce orographic precipitation in the Himalaya and Andes (Bookhagen & Burbank, 2006; Bookhagen & Strecker, 2012). After 8 Ma, flexural modelling shows that relief continued to increase until *ca.* 4.5 Ma, after which it stabilized. Continued development of relief in the Jishi Shan between 8 and 4.5 Ma is also consistent with increased influx of Jishi Shan-sourced sediment into the proximal Linxia Basin (the Wangjiashan location) reflected by increased similarity between basin sediments and northern/northwestern sources (Fig. 10).

CONCLUSIONS

This multidisciplinary study combines sediment provenance, depositional environment reconstruction, stable

isotope geochemistry, and flexural modelling to reconstruct the paleorelief of the Jishi Shan. Detrital zircon U-Pb data document increasing contributions from south–southwest sources including the Qinling Shan and northeast depocenter of the Songpan-Ganzi flysch complex prior to 14 Ma. Exhumation of the Jishi Shan beginning at *ca.* 14 Ma cut off the southern sediment fairways, and resulted in domination of the Linxia Basin record by northern–northwestern sediment sources from 13.1 to *ca.* 8 Ma. Flexural modelling shows that at 13 Ma, the Jishi Shan had developed *ca.* 0.3 km of relief: sufficient to disrupt eastward-flowing drainage networks but insufficient to intercept moisture-bearing airmasses. Hence, the stable isotopic records in the Xunhua and Linxia basins remain coupled until *ca.* 9.3 Ma. Specifically, mean and minimum $\delta^{18}O_c$ values for the interval 10.5–9.3 Ma are indistinguishable in the two basins. We propose that by 9.3 Ma the paleo-Yellow River reestablished its current course, permanently reconnecting the fluvial network between the Xunhua and Linxia basins. Continued exhumation and uplift of the Jishi Shan resulted in sufficient relief to intercept moisture-bearing airmasses at *ca.* 8 Ma, resulting in isolation and aridification of the Xunhua Basin and a decrease in aridity in the Linxia Basin. Flexural modelling indicates that the Jishi Shan had developed *ca.* 0.8 km of relief before triggering this transition. Relief continued to be generated, with >95% of total relief generated by 4.5 Ma. During this time the Jishi Shan continued to be the dominant sediment source for the western Linxia Basin, while the paleo-Yellow River continued to deliver southern and southwestern sourced sediment to the centre of the Linxia Basin.

ACKNOWLEDGEMENTS

We are indebted to Dr. M. Fan for discussions that helped to strengthen and clarify this research. We thank Drs. Hou Sukuan and Li Yikun for their excellent assistance in the field. We thank Dr. R.O. Lease and two anonymous reviewers for their detailed and thoughtful comments, and Dr. G. Hilley for handling this manuscript. We particularly thank Reviewer 3 for a careful second review. Funding for this project was provided by Pioneer Natural Resources, the Chinese Academy of Sciences (Grant No. XDB03020104), the National Natural Sciences Foundation of China (Grant No. 41430102) and the Special Research Program of Basic Science and Technology of the Ministry of Science and Technology (Grant No. 2015FY310100-14). The authors have no conflicts of interest to declare related to this work.

SUPPORTING INFORMATION

Additional Supporting Information may be found in the online version of this article:

Data Repository Text. Detailed zircon U-Pb geochronology methods.

Figure S1. Cumulative compacted and decompacted sediment accumulation curves for the Wangjiashan and Maogou locations since 29 Ma using the alternative chronology of Deng *et al.* (2014).

Table S1. List of samples used in this study.

Table S2. Compaction coefficients.

Table S3. U-Pb data table from University of Houston.

Table S4. U-Pb data table from University of Arizona.

Table S5. MDS results presented in Fig. 10 and 11.

Table S6. Subsidence results presented in Fig. 6.

Table S7. Flexural modelling results presented in Fig. 12.

Data S1. MATLAB (.m) files for MDS algorithm (DZmds).

Data S2. DZmds.exe file.

Data S3. MATLAB (.m) files for flexural modelling.

REFERENCES

Allen, P. & Allen, J. (2005) *Basin Analysis: Principles and Applications.* 2nd edn, Blackwell Scientific Publications, Oxford.

An, Z.-S., Kutzbach, J.E., Prell, W.L. & Porter, S.C. (2001) Evolution of Asian monsoons and phased uplift of the Himalaya-Tibetan Plateau since Late Miocene Times. *Nature*, **311**, 62–66.

Angevine, C., Heller, P. & Paola, C. (1990) Quantitative Sedimentary Basin Modeling, American Association of Petroleum Geologists. Tulsa. Continuing education course note series 32.

Araguas-Araguas, L., Froehlich, K. & Rozanski, K. (1998) Stable isotope composition of precipitation over Southeast Asia. *J. Geophys. Res. Atmos.*, **103**, 28721–28742.

Bershaw, J., Penny, S.M. & Garzione, C.N. (2012) Stable isotopes of modern water across the Himalaya and Eastern Tibetan Plateau: implications for estimates of Paleoelevation and Paleoclimate. *J. Geophys. Res. Atmos.*, **117**, 1–18.

Bershaw, J., Saylor, J.E., Garzione, C.N., Leier, A. & Sundell, K.E. (2016) Stable isotope variations (δ18O and δD) in modern waters across the Andean Plateau. *Geochimica et Cosmochimica Acta*, **194**, 310–324.

Bond, G.C. & Kominiz, M.A. (1984) Construction of tectonic subsidence curves for the Early Paleozoic Miogeocline, Southern Canadian Rocky Mountains: implications for subsidence mechanisms, age of breakup, and crustal thinning. *Geol. Soc. Am. Bull.*, **95**, 155–173.

Bookhagen, B. & Burbank, D.W. (2006) Topography, relief, and trmm-derived rainfall variations along the Himalaya. *Geophys. Res. Lett.*, **33**, 1–5.

Bookhagen, B. & Strecker, M.R. (2012) Spatiotemporal trends in erosion rates across a pronounced rainfall gradient:

examples from the southern Central Andes. *Earth Planet. Sci. Lett.*, **327**, 97–110.

Botsyun, S., Sepulchre, P., Risi, C. & Donnadieu, Y. (2016) Impacts of Tibetan Plateau uplift on atmospheric dynamics and associated precipitation Δ18o. *Clim. Past*, **12**, 1401–1420.

Braitenberg, C., Wang, Y., Fang, J. & Hsu, H.T. (2003) Spatial variations of flexure parameters over the Tibet-Quinghai Plateau. *Earth Planet. Sci. Lett.*, **205**, 211–224.

Bush, M.A., Saylor, J.E., Horton, B.K. & Nie, J. (2016) Growth of the Qaidam Basin During Cenozoic exhumation in the Northern Tibetan Plateau: inferences from depositional patterns and multiproxy detrital provenance signatures. *Lithosphere*, **8**, 58–82.

Cardozo, N. (2016) Backstrip. from http://www.ux.uis.no/~nestor/work/programs.html.

Cardozo, N. (2016) Nestor Cardozo Matlab Scripts. from http://www.ux.uis.no/~nestor/work/matlabScripts.html.

Carroll, A.R., Graham, S.A. & Smith, M.E. (2010) Walled sedimentary basins of China. *Basin Res.*, **22**, 17–32.

CGIRCUG, The College of Geologic Investigation and Research in the Chinese University of Geoscience (2006a) *Geologic Map of Linxia City*. Geologic Maps of the Peoples Republic of China, Geologic Publishing House, Beijing.

CGIRCUG, The College of Geologic Investigation and Research in the Chinese University of Geoscience (2006b) *Geologic Map of Dingxi City*. Geologic Maps of the Peoples Republic of China, Geologic Publishing House, Beijing.

Chen, B., Liu, J., Chen, C., Du, J. & Sun, Y. (2015) Elastic thickness of the Himalayan-Tibetan Orogen estimated from the fan wavelet coherence method, and its implications for lithospheric structure. *Earth Planet. Sci. Lett.*, **409**, 1–14.

Clark, M.K., Farley, K.A., Zheng, D.W., Wang, Z.C. & Duvall, A.R. (2010) Early cenozoic faulting of the Northern Tibetan Plateau Margin from Apatite (U-Th)/He Ages. *Earth Planet. Sci. Lett.*, **296**, 78–88.

Craddock, W.H., Kirby, E. & Zhang, H.P. (2011) Late miocene-pliocene range growth in the interior of the Northeastern Tibetan Plateau. *Lithosphere*, **3**, 420–438.

Dansgaard, W. (1964) Stable isotopes in precipitation. *Tellus*, **16**, 436–468.

Dayem, K.E., Molnar, P., Clark, M.K. & Houseman, G.A. (2009) Far-field lithospheric deformation in tibet during continental collision. *Tectonics*, **28**, 1–9.

DeCelles, P., Kapp, P., Ding, L. & Gehrels, G. (2007) Late cretaceous to middle tertiary basin evolution in the central Tibetan Plateau: changing environments in response to tectonic partitioning, aridification, and regional elevation gain. *Geol. Soc. Am. Bull.*, **119**, 654–680.

Deng, T., Qui, Z.X., Wang, B.Y., Wang, W. & Hou, S.K. (2013) Late cenozoic biostratigraphy of the Linxia Basin, Northwestern China. In: *Fossil Mammals of Asia: Neogene Biostratigraphy and Chronology* (Ed. by X.M. Wang, L. Flynn, M. Fortelius), pp. 243–273. Colombia University Press, New York.

Deng, Y., Zhang, Z., Fan, W. & Pérez-Gussinyé, M. (2014) Multitaper spectral method to estimate the elastic Thickness Of South China: implications for intracontinental deformation. *Geosci. Front.*, **5**, 193–203.

Dettman, D., Fang, X., Garzione, C. & Li, J. (2003) Uplift-driven climate change at 12 Ma: a long delta O-18 record from the Ne margin of the Tibetan Plateau. *Earth Planet. Sci. Lett.*, **214**, 267–277.

Dickinson, W.R. & Gehrels, G.E. (2008) Sediment delivery to the cordilleran foreland basin: insights from U-Pb ages of Detrital Zircons in Upper Jurassic and Cretaceous Strata of the Colorado Plateau. *Am. J. Sci.*, **308**, 1041–1082.

Duvall, A.R., Clark, M.K., van der Pluijm, B. & Li, C.Y. (2011) Direct dating of eocene reverse faulting in Northeastern Tibet Using Ar-Dating of fault clays and low-temperature thermochronometry. *Earth Planet. Sci. Lett.*, **304**, 520–526.

Duvall, A.R., Clark, M.K., Kirby, E., Farley, K.A., Craddock, W.H., Li, C. & Yuan, D.-Y. (2013) Low-temperature thermochronometry along the Kunlun and Haiyuan Faults, Ne Tibetan Plateau: evidence for kinematic change during late-stage orogenesis. *Tectonics*, **32**, 1190–1211.

Fan, M.J., Dettman, D.L., Song, C.H., Fang, X.M. & Garzione, C.N. (2007) Climatic variation in the Linxia Basin, Ne Tibetan Plateau, from 13.1 to 4.3 Ma: The Stable Isotope Record. *Palaeogeogr. Palaeoclimatol. Palaeoecol.*, **247**, 313–328.

Fang, X., Li, J., Zhu, J., Cheng, H. & Cao, J. (1997) Determination and calibration of time scale of late cenozoic sedimentary sequences in Linxia Basin, Gansu Province, China. *Chin. Sci. Bull.*, **42**, 1457–1471.

Fang, X.-M., Garzione, C., Van der Voo, R., Li, J.-J. & Fan, M.-J. (2003) Flexural subsidence by 29 Ma on the Ne Edge of Tibet from the Magnetostratigraphy of Linxia Basin, China. *Earth Planet. Sci. Lett.*, **210**, 545–560.

Fosdick, J.C., Graham, S.A. & Hilley, G.E. (2014) Influence of attenuated lithosphere and sediment loading on flexure of the deep-water magallanes retroarc foreland Basin, Southern Andes. *Tectonics*, **33**, 2505–2525.

Garzione, C.N., Ikari, M.J. & Basu, A.R. (2005) Source of oligocene to pliocene sedimentary rocks in the Linxia Basin in Northeastern Tibet from Nd Isotopes: implications for tectonic forcing of climate. *Geol. Soc. Am. Bull.*, **117**, 1156–1166.

GBGMR, Gansu Bureau of Geology and Mineral Resources (1989) *Regional Geology of Gansu Province*, Geological Publishing House, Beijing. 692 p.

Gehrels, G.E., Valencia, V.A. & Ruiz, J. (2008) Enhanced precision, accuracy, efficiency, and spatial resolution of U-Pb Ages by Laser Ablation-Multicollector-inductively coupled plasma-mass spectrometry. *Geochem. Geophys. Geosyst.*, **9**, 1–13.

Gu, Z.G., Wang, S.H., Hsu, S.Y. & Wei, D.T. (1995a) Research progress on biostratigraphy of tertiary red beds in Linxia Basin, Gansu Province. In: *Study on the Formation and Evolution of the Qinghai-Xizang Province: Environmental Change Nad Ecological System* (Ed. by The Expert Committee on Qingzang Program), pp. 91–95. Science Press, Beijing.

Gu, Z.G., Wang, S.H., Hsu, S.Y. & Wei, D.T. (1995b) Discovery of giraffokeryx in China and the tertiary chronostratigraphy of Linxia, Gansu Province. *China Sci. Bull.*, **40**, 758–760.

Hetenyi, M. (1979) *Beams on Elastic Foundation*. University of Michigan Press, Ann Arbor.

Horton, B.K. (2012) Cenozoic evolution of Hinterland Basins in the Andes and Tibet. In: *Recent Advances in Tectonics of*

Sedimentary Basins (Ed. by C.J. Busby & A. Azor), pp. 427–444. Wiley-Blackwell, Oxford, UK.

Horton, B.K., Dupont-Nivet, G., Zhou, J., Waanders, G.L., Butler, R.F. & Wang, J. (2004) Mesozoic-cenozoic evolution of the Xining-Minhe and Dangchang Basins, Northeastern Tibetan Plateau: magnetostratigraphic and biostratigraphic results. *J. Geophys. Res. Solid Earth*, **109**, 1–15.

Hough, B.G., Garzione, C.N., Wang, Z.C., Lease, R.O., Burbank, D.W. & Yuan, D.Y. (2011) Stable isotope evidence for topographic growth and basin segmentation: implications for the evolution of the Ne Tibetan Plateau. *Geol. Soc. Am. Bull.*, **123**, 168–185.

Hough, B. G., Garzione, C. N., Wang, Z. & Lease, R. O. (2014) Timing and spatial patterns of basin segmentation and climate change in northeastern Tibet. In: *Toward an Improved Understanding of Uplift Mechanisms and the Elevation History of the Tibetan Plateau* (Ed. by Nie, J., Horton, B. K., & Hoke, G. D.) *Geol. Soc. Am. Spl. Pap.*, **507**, 129–153.

Hren, M.T., Bookhagen, B., Blisniuk, P.M., Booth, A.L. & Chamberlain, C.P. (2009) Delta O-18 and delta D of streamwaters across the Himalaya and Tibetan Plateau: implications for moisture sources and paleoelevation reconstructions. *Earth Planet. Sci. Lett.*, **288**, 20–32.

Jordan, T.E. (1981) Thrust loads and foreland basin evolution, Cretaceous, Western United States. *Am. Asso. Petrol. Geol. Bull.*, **65**, 2506–2520.

Jordan, T. & Watts, A. (2005) Gravity anomalies, flexure and the elastic thickness structure of the India-Eurasia Collisional System. *Earth Planet. Sci. Lett.*, **236**, 732–750.

Kent-Corson, M.L., Ritts, B.D., Zhuang, G.S., Bovet, P.M., Graham, S.A. & Chamberlain, C.P. (2009) Stable isotopic constraints on the tectonic, topographic, and climatic evolution of the Northern Margin of the Tibetan Plateau. *Earth Planet. Sci. Lett.*, **282**, 158–166.

Kleinert, K. & Strecker, M.R. (2001) Climate change in response to orographic barrier uplift: paleosol and stable isotope evidence from the late Neogene Santa Maria basin, northwestern Argentina. *Geol. Soci. Am. Bull.*, **113**, 728–742.

Lease, R.O. (2014) Cenozoic mountain building on the Northeastern Tibetan Plateau. *Geol. Soc. Am. Spec. Pap.*, **507**, 115–127.

Lease, R.O., Burbank, D.W., Gehrels, G.E., Wang, Z.C. & Yuan, D.Y. (2007) Signatures of mountain building: detrital zircon U/Pb Ages from Northeastern Tibet. *Geology*, **35**, 239–242.

Lease, R.O., Burbank, D.W., Clark, M.K., Farley, K.A., Zheng, D.W. & Zhang, H.P. (2011) Middle miocene reorganization of deformation along the Northeastern Tibetan Plateau. *Geology*, **39**, 359–362.

Lease, R.O., Burbank, D.W., Hough, B., Wang, Z.C. & Yuan, D.Y. (2012a) Pulsed Miocene range growth in Northeastern Tibet: insights from Xunhua Basin Magnetostratigraphy and Provenance. *Geol. Soc. Am. Bull.*, **124**, 657–677.

Lease, R.O., Burbank, D.W., Zhang, H., Liu, J. & Yuan, D. (2012b) Cenozoic shortening budget for the Northeastern Edge of the Tibetan Plateau: is lower crustal flow necessary? *Tectonics*, **31**, 1–16.

Leier, A., Quade, J., DeCelles, P. & Kapp, P. (2009) Stable isotopic results from Paleosol Carbonate in South Asia: paleoenvironmental reconstructions and selective alteration. *Earth Planet. Sci. Lett.*, **279**, 242–254.

Li, L., Garzione, C.N., Pullen, A. & Chang, H. (2016) Early-middle miocene topographic growth of the Northern Tibetan Plateau: stable isotope and sedimentation evidence from the Southwestern Qaidam Basin. *Palaeogeogr. Palaeoclimatol. Palaeoecol.*, **461**, 201–213.

Liu, S.F., Zhang, G.W., Pan, F., Zhang, H.P., Wang, P., Wang, K. & Wang, Y. (2013) Timing of Xunhua and Guide Basin development and growth of the Northeastern Tibetan Plateau, China. *Basin Res.*, **25**, 1–23.

Metivier, F., Gaudemer, Y., Tapponnier, P. & Meyer, B. (1998) Northeastward growth of the Tibet Plateau deduced from balanced reconstruction of two depositional areas: The Qaidam and Hexi Corridor Basins, China. *Tectonics*, **17**, 823–842.

Meyer, B., Tapponnier, P., Bourjot, L., Metivier, F., Gaudemer, Y., Peltzer, G., Shunmin, G. & Zhitai, C. (1998) Crustal thickening in Gansu-Qinghai, Lithospheric Mantle Subduction, and Oblique, strike-slip controlled growth of the Tibet Plateau. *Geophys. J. Int.*, **135**, 1–47.

Nie, J., Stevens, T., Rittner, M., Stockli, D., Garzanti, E., Limonta, M., Bird, A., Andò, S., Vermeesch, P., Saylor, J., Lu, H., Breecker, D., Hu, X., Liu, S., Resentini, A., Vezzoli, G., Peng, W., Carter, A., Ji, S. & Pan, B. (2015) Loess plateau storage of Northeastern Tibetan Plateau-Derived yellow river sediment. *Nat. Commun.*, **6**, 8511.

Pingel, H., Alonso, R.N., Mulch, A., Rohrmann, A., Sudo, M. & Strecker, M.R. (2014) Pliocene orographic barrier uplift in the Southern Central andes. *Geology*, **42**, 691–694.

Poulsen, C.J. & Jeffery, M.L. (2011) Climate change imprinting on stable isotopic compositions of high-elevation meteoric water cloaks past surface elevations of Major Orogens. *Geology*, **39**, 595–598.

QBGMR, Qinghai Bureau of Geology and Mineral Resources (1991) *Regional Geology of Qinghai Province*. Beijing Geological Publishing House, Beijing.

Qiu, Z.-X. & Qiu, Z.-D. (1990) The sequence and division of mammalian local faunas in the Neogene of China. *J. Stratigr.*, **14**, 241–260.

Qiu, Z.X., Xie, H.Y. & Yan, D.F. (1990) Discovery of some early miocene mammalian fossils from Dongxiang, Gansu. *Vertebrate Palasiatica*, **28**, 24.

Qiu, Z.-X., Wang, B.-Y., Deng, T., Ni, X.-J. & Wang, X. (2002) Notes on the mammal fauna from the bottom of loess deposits at Longdan, Dongxiang County, Gansu Province. *Quat. Sci.*, **22**, 33–38.

Quade, J., Garzione, C. & Eiler, J. (2007) Paleoelevation reconstruction using pedogenic carbonates. In: *Paleoaltimetry: Geochemical and Thermodynamic Approaches* (Ed. by M.J. Kohn) *Rev. Mineral. Geochem.*, **66**, 53–87.

Quade, J., Breecker, D.O., Daeron, M. & Eiler, J. (2011) The paleoaltimetry of tibet: an isotopic perspective. *Am. J. Sci.*, **311**, 77–115.

Rowley, D.B. (2007) Stable isotope-based paleoaltimetry: theory and validation. In: *Paleoaltimetry: Geochemical and Thermodynamic Approaches* (Ed. by M.J. Kohn) *Rev. Mineral. Geochem.*, **66**, 23–52. Mineralogical Soc Amer, Chantilly.

Rozanski, K., Araguas-Araguas, L. & Gonfiantini, R. (1993) Isotopic patterns in modem global precipitation. In: *Climate*

Change in Continental Isotopic Records - Geophysical Monograph 78 (Ed. by P.K. Swart, K.C. Lohman, J. McKenzie, S. Savin), pp. 1–36. American Geophysical Union, Washington, D.C.

Saylor, J.E. & Sundell, K.E. (2016) Quantifying comparison of large detrital geochronology data sets. *Geosphere*, **12**, 203–220.

Saylor, J.E., Stockli, D.F., Horton, B.K., Nie, J. & Mora, A. (2012) Discriminating rapid exhumation from syndepositional volcanism using detrital zircon double dating: implications for the tectonic history of the Eastern Cordillera, Colombia. *Geol. Soc. Am. Bull.*, **124**, 762–779.

Saylor, J.E., Knowles, J.N., Horton, B.K., Nie, J.S. & Mora, A. (2013) Mixing of source populations recorded in Detrital Zircon U-Pb Age Spectra of Modern River Sands. *J. Geol.*, **121**, 17–33.

Sclater, J.G. & Christie, P.A.F. (1980) Continental stretching: an explanation of the post-mid-cretaceous subsidence of the Central North Sea Basin. *J. Geophys. Res. Solid Earth*, **85**, 3711–3739.

Sircombe, K.N. (2004) Agedisplay: an excel workbook to evaluate and display univariate geochronological data using binned frequency histograms and probability density distributions. *Comput. Geosci.*, **30**, 21–31.

Sobel, E.R., Hilley, G.E. & Strecker, M.R. (2003) Formation of internally drained contractional basins by aridity-limited bedrock incision. *J. Geophys. Res. Solid Earth*, **108**, 1–23.

Strecker, M.R., Alonso, R.N., Bookhagen, B., Carrapa, B., Hilley, G.E., Sobel, E.R. & Trauth, M.H. (2007) Tectonics and Climate of the Southern Central Andes. *Annu. Rev. Earth Planet. Sci.*, **35**, 747–787.

Sun, C.R., Chen, G.L. & Li, Z.R. (1997) Stratigraphy (Lithostratic) of Qinghai Province (in Chinese). University of Geosciences Press, Wuhan, China.

Tang, H., Micheels, A., Eronen, J.T., Ahrens, B. & Fortelius, M. (2013) Asynchronous responses of East Asian and Indian summer monsoons to mountain uplift shown by regional climate modelling experiments. *Clim. Dyn.*, **40**, 1531–1549.

Tapponnier, P., Xu, Z.Q., Roger, F., Meyer, B., Arnaud, N., Wittlinger, G. & Yang, J.S. (2001) Geology - oblique stepwise rise and growth of the Tibet Plateau. *Science*, **294**, 1671–1677.

Taylor, M., Yin, A., Ryerson, F., Kapp, P. & Ding, L. (2003) Conjugate strike-slip faulting along the Bangong-Nujiang Suture Zone Accommodates Coeval East-West Extension and North-South Shortening in the Interior of the Tibetan Plateau. *Tectonics*, **22**, 1–16.

Tian, L., Yao, T., Numaguti, A. & Sun, W. (2001) Stable isotope variations in monsoon precipitation on the Tibetan Plateau. *J. Meteorol. Soc. Jpn*, **79**, 959–966.

Tian, L., Yao, T., MacClune, K., White, J.W.C., Schilla, A., Vaughn, B., Vachon, R. & Ichiyanagi, K. (2007) Stable isotopic variations in West China: a consideration of moisture sources. *J. Geophys. Res. Atmos.*, **112**, 1–12.

Turcotte, D.L. & Schubert, G. (1982) *Geodynamics*. Cambridge University Press, Cambridge.

Vermeesch, P. (2013) Multi-sample comparison of detrital age distributions. *Chem. Geol.*, **341**, 140–146.

Vuille, M., Bradley, R.S., Werner, M., Healy, R. & Keimig, F. (2003) Modeling Δ18o in precipitation over the tropical Americas: 1. Interannual variability and climatic controls. *J. Geophys. Res. Atmos.*, **108**, 1–24.

Vuille, M., Werner, M., Bradley, R.S. & Keimig, F. (2005) Stable isotopes in precipitation in the Asian Monsoon Region. *J. Geophys. Res. Atmos.*, **110**, 1–15.

Wangen, M. (2010) *Physical Principles of Sedimentary Basin Analysis*. Cambridge University Press, Cambridge.

Watts, A.B. (2001) *Isostasy and Flexure of the Lthosphere*. Cambridge University Press, Cambridge.

Weislogel, A.L., Graham, S.A., Chang, E.Z., Wooden, J.L. & Gehrels, G.E. (2010) Detrital Zircon Provenance from Three Turbidite Depocenters of the middle-upper triassic Songpan-Ganzi complex, Central China: record of collisional tectonics, erosional exhumation, and sediment production. *Geol. Soc. Am. Bull.*, **122**, 2041–2062.

Yong, L., Allen, P.A., Densmore, A.L. & Qiang, X. (2003) Evolution of the Longmen Shan Foreland Basin (Western Sichuan, China) During the Late Triassic Indosinian Orogeny. *Basin Res.*, **15**, 117–138.

Yuan, D.-Y., Ge, W.-P., Chen, Z.-W., Li, C.-Y., Wang, Z.-C., Zhang, H.-P., Zhang, P.-Z., Zheng, D.-W., Zheng, W.-J., Craddock, W.H., Dayem, K.E., Duvall, A.R., Hough, B.G., Lease, R.O., Champagnac, J.-D., Burbank, D.W., Clark, M.K., Farley, K.A., Garzione, C.N., Kirby, E., Molnar, P. & Roe, G.H. (2013) The Growth of Northeastern Tibet and its relevance to large-scale continental geodynamics: a review of recent studies. *Tectonics*, **32**, 2013TC003348.

Zhuang, G., Brandon, M.T., Pagani, M. & Krishnan, S. (2014) Leaf wax stable isotopes from Northern Tibetan Plateau: implications for uplift and Climate since 15 Ma. *Earth Planet. Sci. Lett.*, **390**, 186–198.

Manuscript received 4 December 2016; In revised form 13 August 2017; Manuscript accepted 27 August 2017.